

# Supporting Information for:

## Luminescence, Chiroptical, Magnetic and Ab-initio Crystal-Field Characterizations of an Enantiopure Helicoidal Yb(III) Complex

Frédéric Gendron,<sup>a,#</sup> Sebastiano Di Pietro,<sup>b,#</sup> Laura Abad Galan,<sup>b</sup> François Riobé,<sup>b</sup> Virginie Placide,<sup>b</sup> Laure Guy,<sup>b</sup> Francesco Zinna,<sup>c</sup> Lorenzo Di Bari,<sup>c,\*</sup> Amina Bensalah-Ledoux,<sup>d</sup> Yannick Guyot,<sup>d</sup> Guillaume Pilet,<sup>e</sup> Fabrice Pointillart,<sup>a</sup> Bruno Baguenard,<sup>d</sup> Stephan Guy,<sup>d,\*</sup> Olivier Cador,<sup>a</sup> Olivier Maury,<sup>b,\*</sup> Boris Le Guennic<sup>a,\*</sup>

[a] Dr. F. Gendron, Dr. F. Pointillart, Pr. O. Cador, Dr. B. Le Guennic

Univ. Rennes, CNRS, ISCR (Institut des Sciences Chimiques de Rennes) - UMR 6226, F-35000 Rennes (France)

E-mail: boris.leguennic@univ-rennes1.fr

[b] Dr. S. Di Pietro, Dr. L. Abad Gallan, Dr. F. Riobé, Dr. L. Guy, Dr. O. Maury

Univ. Lyon, ENS de Lyon, CNRS Laboratoire de Chimie UMR 5182, Université Claude Bernard Lyon 1, F-69342 Lyon, France.

E-mail: olivier.maury@ens-lyon.fr

[c] Dr. F. Zinna, Pr. L. Di Bari

Dipartimento di Chimica e Chimica Industriale, Università di Pisa, via Moruzzi 13, 56124 Pisa (Italy)

E-mail: lorenzo.dibari@unipi.it

[d] Dr. B. Baguenard, Dr. A. Bensalah-Ledoux, Pr. S. Guy, Dr. Y. Guyot

Univ. Lyon, Institut Lumière Matière, UMR 5306 CNRS–Université Claude Bernard Lyon 1, 10 rue Ada Byron, 69622 Villeurbanne Cedex, France. E-mail: Stephan.guy@univ-lyon1.fr

[e] Dr. G. Pilet

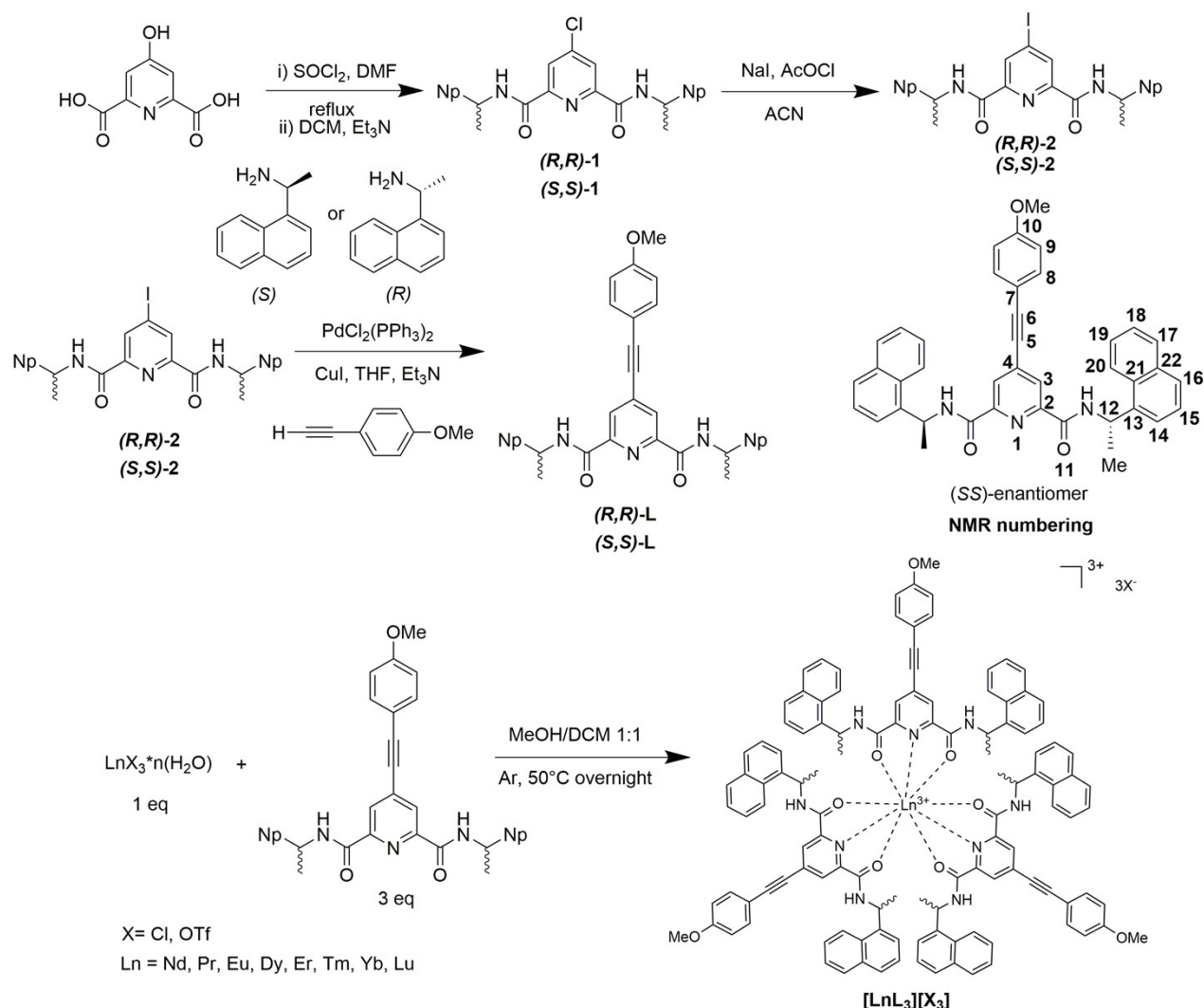
Univ. Lyon, Laboratoire des Multimatériaux et Interfaces (LMI), UMR 5615 CNRS-Université Claude Bernard Lyon 1, 43 boulevard du 11 novembre 1918, 69622 Villeurbanne cedex, France.

# These authors contributed equally to the work.

### Content.

- 1) Synthesis and characterization
- 2) X-ray diffraction data
- 3) Magnetic measurements
- 4) Photophysics and chiroptics
- 5) Computational details
- 6) Paramagnetic NMR analysis and solution structure calculation
- 7) NMR spectra

## 1) Synthesis and characterization.



**Scheme S1.** Synthetic pathway for the preparation of the  $(R,R)$ - and  $(S,S)$ -L ligands and the  $[\text{Ln}(R,R)\text{-L}_3](\text{OTf})_3$  relative complexes. The NMR labels are also illustrated.

**General.** Solvents and starting materials were purchased from Sigma-Aldrich or TCI and used without further purification, unless otherwise stated. Lanthanide chloride, triflate and nitrate salts were purchased from Aldrich. Solvents were dried and purified using standard techniques. Flash chromatography was performed with analytical-grade solvents using Aldrich silica gel (technical grade, pore size 60 Å, 230-400 mesh particle size). Flexible plates ALUGRAM® Xtra SIL G UV254 from MACHEREY-NAGEL were used for TLC. Compounds were detected by UV irradiation (Bioblock Scientific). NMR spectra were recorded with a Bruker AVANCE III 300 ( $^1\text{H}$ , 300 MHz and  $^{13}\text{C}$ , 75 MHz) or a Bruker AVANCE DRX500 ( $^1\text{H}$ , 500 MHz;  $^{13}\text{C}$ , 125 MHz).

Chemical shifts are given in ppm relative to TMS and coupling constants J in Hz. High resolution mass spectroscopy measurements were performed at Centre Commun de Spectrométrie de Masse (Villeurbanne, France). Column chromatography was performed using Acros Oorganics (0.035-0.70 mm) silicagel. The reaction apparatus, when required, was oven dried, cooled down under vacuum and then argon filled after at least 3× cycle of vacuum/argon.

**(R,R)- and (S,S)-1.** Under argon, 500 mg of chelidamic acid (2.49 mmol, 1 eq) were dissolved in 50 ml of thionyl chloride in a 100 ml two-neck flask. Then, 0.3 ml of anhydrous DMF were added while the suspension was stirred at 0°C with an ice/water bath. The mixture was refluxed at 80°C overnight. Then, the solvent was carefully evaporated using twice 10 ml of toluene, and the remaining solid was dissolved in dichloromethane (10 ml), under argon. A solution of the chiral enantiopure (**R**)-(+)- or (**S**)-(-)- 1-(1-Naphthyl)ethylamine (2.5 eq) in 1 ml of triethylamine (3.2 eq) was slowly added at 0°C. The orange mixture was stirred at room temperature overnight. Then, a 1M solution of K<sub>2</sub>CO<sub>3</sub> was added until pH = 10. The organic solution was extract and washed twice with water, once with brine and dried with anhydrous magnesium sulphate. And the solvents were evaporated under vacuum after filtration. The crude product was purified by flash chromatography (Al<sub>2</sub>O<sub>3</sub> activity III, dichloromethane/ethyl acetate 98:2) to afford both the enantiomer products in 70% yield.<sup>1</sup>H-NMR (500 MHz, CDCl<sub>3</sub>) δ = 8.24 (s, 2H), 8.07 (d, 2H, <sup>3</sup>J = 8.4 Hz), 7.92 (d, 2H, <sup>3</sup>J = 7.3 Hz), 7.84 (d, 2H), 7.74 (d, 2H, <sup>3</sup>J = 7.3 Hz), 7.51 (m, 4H), 7.35 (m, 4H), 5.94 (quintuplet, 2H), 1.53 (d, 6H, <sup>3</sup>J = 6.7 Hz). <sup>13</sup>C-NMR (125 MHz, CDCl<sub>3</sub>) δ = 162.42, 149.90, 147.45, 137.82, 133.83, 130.82, 128.89, 128.40, 126.63, 125.90, 125.44, 125.44, 125.09, 123.10, 122.62, 45.30, 20.81. HRMS (ESI): found 508.1783 m/z, calculated for C<sub>31</sub>H<sub>26</sub>ClN<sub>3</sub>O<sub>2</sub> 508.1786 m/z [M+H]<sup>+</sup>.

**(S,S)- and (R,R)-2.** 400 mg of (**S,S**)- or (**R,R**)-**1** (0.77 mmol, 1 eq) and 1.2 g of sodium iodide (7.68 mmol, 10 eq) were dissolved/suspended in 50 ml of acetonitrile and sonicated for 1 h. Then, 450 µl of acetyl chloride (8 eq, 6.3 mmol) were added dropwise. The mixture was sonicated for other 2 h. Then, the suspension was extracted with 50 ml of dichloromethane and successively washed with a saturated Na<sub>2</sub>CO<sub>3</sub> solution, a 0.1 M solution of sodium thiosulphate, water (until pH = 7) and finally brine. The organic solution was then dried with anhydrous sodium sulphate, filtrated and the solvent evaporated. The crude product was recrystallized from hot methanol affording both the enantiomer product with 70-75% yields. <sup>1</sup>H-NMR (500 MHz, CDCl<sub>3</sub>) δ = 8.69 (s, 2H), 8.11 (m, 2H), 7.89 (m, 2H), 7.82 (dd, 2H, <sup>3</sup>J = 6.9 Hz, <sup>4</sup>J = 2.3 Hz), 7.70 (d, 2H, <sup>3</sup>J = 8.2 Hz), 7.52 (m, 4H), 7.41 (m, 4H), 6.00 (quintuplet, 2H), 1.63 (d, 6H, <sup>3</sup>J =

6.7 Hz).  $^{13}\text{C}$ -NMR (125 MHz,  $\text{CDCl}_3$ )  $\delta$  = 161.19, 148.66, 137.82, 134.52, 133.95, 130.92, 128.95, 128.56. HMRS (ESI): found 600.1143, calculated for  $\text{C}_{31}\text{H}_{26}\text{IN}_3\text{O}_2$  600.1142  $[\text{M}+\text{H}]^+$ .

**(*R,R*)-L** and **(*S,S*)-L**. In a two-neck balloon under argon atmosphere, 200 mg of (*R,R*)- or (*S,S*)-**2** (0.33 mmol, 1 eq) were dissolved in 30 ml of anhydrous tetrahydrofuran and argon was bubbled for 30 min. Then, 23 mg of  $\text{PdCl}_2(\text{PPh}_3)_2$  (0.033 mmol, 0.1 eq) and 13 mg of  $\text{CuI}$  (0.066 mmol, 0.2eq) were added. As last, 70 mg of 4-ethynylanisole (0.495 mmol, 1.5 eq) dissolved in 10 ml of triethylamine were added and the mixture was refluxed under argon overnight. Then, the solution was cooled down at room temperature, filtered through a celite pad, dichloromethane was added and the organic phase was washed with saturated ammonium chloride, water and brine, dried with anhydrous sodium sulphate, filtered and the solvent evaporated. The crude product was purified by a  $\text{SiO}_2$  pad using as first dichloromethane to clean from the 4-ethynylanisole excess and as last ethyl acetate to recover the clean product in quantitative yield for both the enantiomers (200 mg, Yield = quantitative) as a yellow powder.  $^1\text{H}$ -NMR (300 MHz,  $\text{CDCl}_3$ )  $\delta$  = 8.37 (s, 2H), 8.16 (m, 2H), 7.90 (m, 2H), 7.84 (m, 2H), 7.72 (d, 2H,  $^3\text{J}$  = 8 Hz), 7.52-7.44 (m, 10H), 6.91 (d, 2H,  $^3\text{J}$  = 9 Hz), 6.04 (quintuplet, 2H), 3.85 (s, 3H), 1.66 (d, 6H,  $^3\text{J}$  = 7 Hz).  $^{13}\text{C}$ -NMR (125 MHz,  $\text{CDCl}_3$ )  $\delta$  = 162.26, 160.86, 148.94, 138.23, 135.40, 134.11, 133.96, 131.10, 129.07, 128.62, 126.80, 126.09, 125.39, 123.44, 122.86, 114.40, 113.78, 97.29, 85.35, 55.52, 45.42, 21.12. HRMS (ESI), found for (*R,R*)- enantiomer 604.2602  $[\text{M}+\text{H}]^+$  and 626.2416  $[\text{M}+\text{Na}]^+$ , calculated for  $\text{C}_{40}\text{H}_{34}\text{N}_3\text{O}_3$  604.2595 and for  $\text{C}_{40}\text{H}_{33}\text{N}_3\text{NaO}_3$  626.2414; for the (*S,S*)- enantiomer 604.2601  $[\text{M}+\text{H}]^+$  and 626.2415  $[\text{M}+\text{Na}]^+$ , calculated for  $\text{C}_{40}\text{H}_{34}\text{N}_3\text{O}_3$  604.2595 and for  $\text{C}_{40}\text{H}_{33}\text{N}_3\text{NaO}_3$  626.2414.

**General complexation procedure:** 3 eq of the desired ligand were dissolved in a 1:1 mixture of dichloromethane and methanol under argon atmosphere. Then, 1 eq of lanthanide salt (triflate or chloride or nitrate just for the Dysprosium complexes) was added. The solution is stirred under argon at 50°C overnight to assure a complete complexation. Then, it is cooled down and the solvent evaporated. The clean complex is precipitated from methanol using diethylether as non-solvent. The solid is collected through filtration on a glass filter, washed with diethylether and dried to obtain a yellowish powder. The complexes were characterized by  $^1\text{H}$ - and  $^{13}\text{C}$ -NMR and HR-MS. Details of the NMR characterization and spectra are given in SI part 6 and 7.

**$[\text{Yb}(\text{S,S})\text{-L}_3](\text{OTf})_3$ .** Following the general procedure, 40 mg of (*S,S*)-**L** (0.066 mmol, 3 eq) in 40 ml of a 1:1 mixture methanol/dichloromethane, with 13.6 mg of  $\text{Yb}(\text{OTf})_3$  (0.022 mmol, 1 eq) to afford 20.23 mg of complex (Yield = 46%).  $^1\text{H}$ -NMR (500 MHz,  $\text{CD}_3\text{OD}$ ),  $\delta$  = 15.05, 13.13, 9.2, 7.35, 6.96, 6.78, 6.57, 5.51, 4.38, 3.7, 2.84, 2.26, 3.3.  $^{13}\text{C}$ -NMR (125 MHz,  $\text{CD}_3\text{OD}$ )  $\delta$  =

134.15, 129.98, 128.63, 126.74, 126.06, 124.73, 122.5, 116.33, 115.43, 112.82, 55.62, 23.52. HRMS (ESI), found 661.2301 [M]<sup>3+</sup>, calculated for [C<sub>120</sub>H<sub>99</sub>N<sub>9</sub>O<sub>9</sub>Yb]<sup>3+</sup> 661.2313.

**[Yb(*R,R*)-L<sub>3</sub>](OTf)<sub>3</sub>.** Following the general procedure, 40 mg of (*R,R*)-L (0.066 mmol, 3 eq) in 40 ml of a 1:1 mixture methanol/dichloromethane, with 13.6 mg of Yb(OTf)<sub>3</sub> (0.022 mmol, 1 eq) to afford 39.25 mg of complex (Yield = 89%). For <sup>1</sup>H- and <sup>13</sup>C-NMR spectra peaks list see the other enantiomer. HRMS (ESI), found 661.2303 [M]<sup>3+</sup>, calculated for [C<sub>120</sub>H<sub>99</sub>N<sub>9</sub>O<sub>9</sub>Yb]<sup>3+</sup> 661.2313.

## 2) X-ray diffraction data.

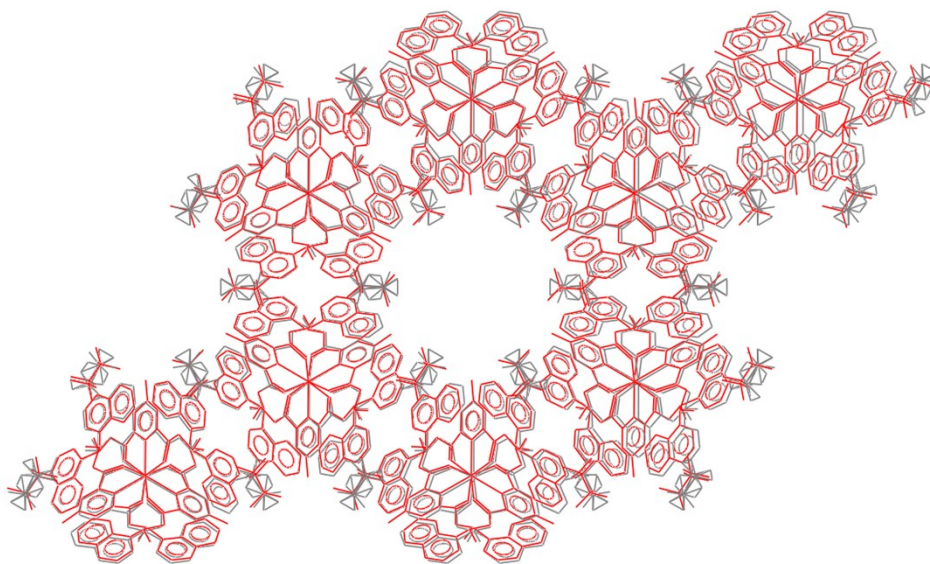


**Figure S1.** Overlay of the [Er(*R,R*)-L<sub>3</sub>](OTf)<sub>3</sub> X-ray structure (viewed along c axis) with the one of the parent Tb complex obtained with dinaphthyl-dipicamide, previously reported in ref. [1].

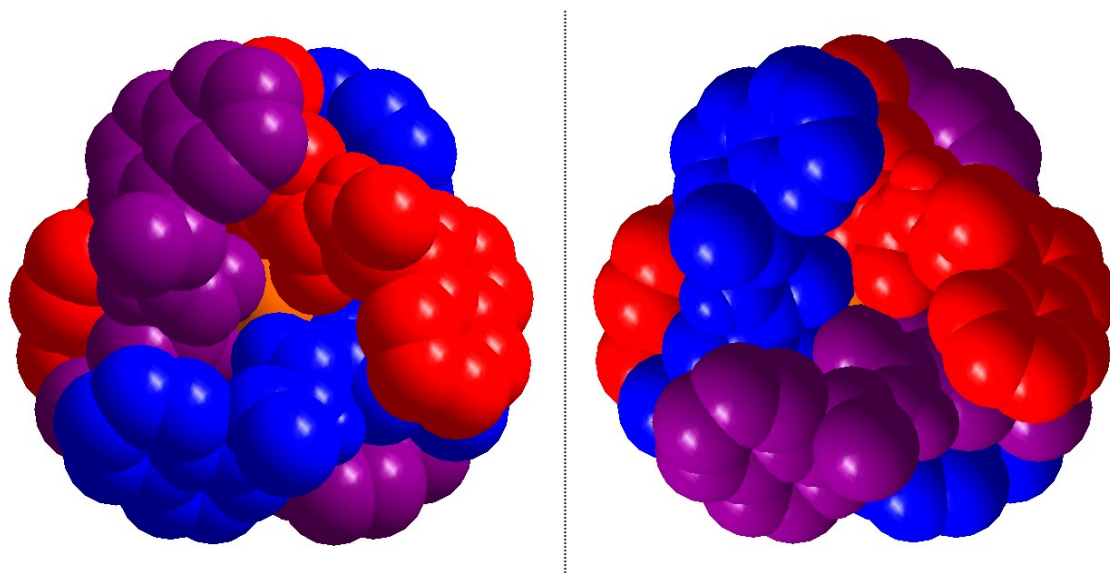


**Figure S2.** Views of the  $\Lambda$ -helicity of the ligand wrapping observed in the X-ray structure of  $[\text{Er}(\mathbf{R},\mathbf{R})\text{-L}_3](\text{OTf})_3$  along both directions of the  $c$  crystallographic axis.

The comparison of the PERSEUS structure, with the one reported by Gunnlaugsson and the partial X-ray structure characterized for this work is reported in Table S1.

**Table S1.** Comparison between angles (in degree) in different structures.

	$\alpha$	$\psi$	C11-N-C12-C13	Me-C12-C13-C21
<b>PERSEUS</b> $[\text{Yb}(\mathbf{R},\mathbf{R})\text{-L}_3]^{3+}$	14.4	44	85	79
$[\text{Er}(\mathbf{R},\mathbf{R})\text{-L}_3](\text{OTf})_3$	13.1	51	86.3/59.9	96.5/82.4
<b>Gunnlaugsson</b> <sup>1</sup>	14.2	49	74.9	82

The polyhedron ( $\alpha$  and  $\psi$  angles) seemed to be quite close among the three different structures even if the overall symmetry is different ( $D_3$  for the PERSEUS one and lower for the two others). Some small differences are appreciable in the arrangement of the C11-N-C12-C13 chain (and Me-C12-C13-C21) whose dihedral angle is responsible for the orientation of the naphthyl moieties. Interestingly, aside for the overall symmetry and the packing effect the core of the coordination motif around the lanthanide ions is very similar in these three structures and it represents a strong proof of isostructurality not only in solution among the different lanthanide derivatives of **L**, but also between solid and solution state.

### 3) Magnetic measurements

The static magnetic measurements ( $\chi_M T$  vs.  $T$  and  $M$  vs.  $H$ ) have been performed on a Quantum Design PPMS magnetometer on immobilized microcrystallites in Teflon tape pellet. The molar magnetic susceptibility,  $\chi_M$  has been recorded at 2 kOe between 2 and 20 K and at 10 kOe for higher temperatures. The linearity of the magnetization with respect to the magnetic field has been verified at 20 and 300 K. The dynamic magnetic measurements have been performed on the same pellet with a Quantum Design PPMS equipped with ACMS-II option for 5 Oe oscillating fields at frequencies between 100 and 10000 Hz.

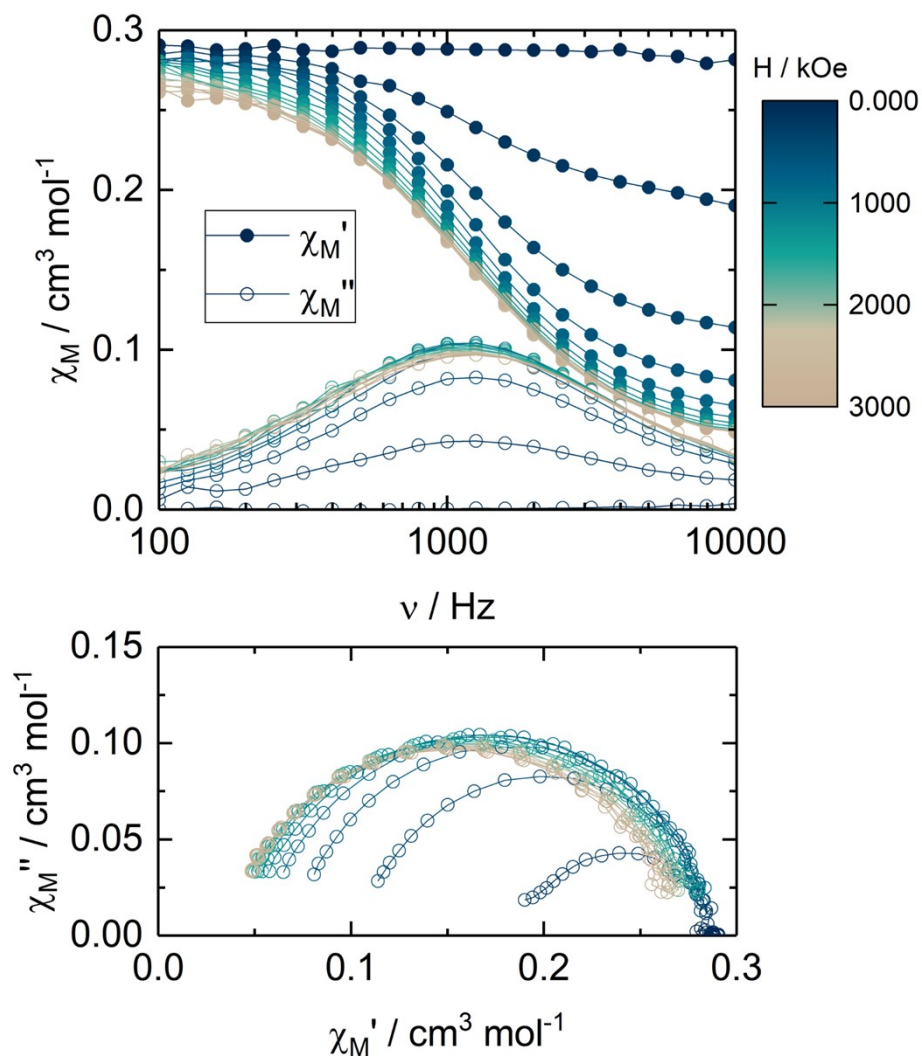


**Figure S3.** (top) Frequency dependences of both in-phase ( $\chi_M'$ ) and out-of-phase ( $\chi_M''$ ) components of the ac molar magnetic susceptibility at 2 K and at various external dc fields for  $[\text{Yb}(\mathbf{S},\mathbf{S})\text{-L}_3](\text{OTf})_3$ . (bottom) Argand representation of the top figure.

**Extended Debye model.**

$$\chi_M' = \chi_S + (\chi_T - \chi_S) \frac{1 + (\omega\tau)^{1-\alpha} \sin\left(\alpha \frac{\pi}{2}\right)}{1 + 2(\omega\tau)^{1-\alpha} \sin\left(\alpha \frac{\pi}{2}\right) + (\omega\tau)^{2-2\alpha}}$$

$$\chi_M'' = (\chi_T - \chi_S) \frac{(\omega\tau)^{1-\alpha} \cos\left(\alpha \frac{\pi}{2}\right)}{1 + 2(\omega\tau)^{1-\alpha} \sin\left(\alpha \frac{\pi}{2}\right) + (\omega\tau)^{2-2\alpha}}$$

With  $\chi_T$  the isothermal susceptibility,  $\chi_S$  the adiabatic susceptibility,  $\tau$  the relaxation time and  $\alpha$  an empiric parameter which describe the distribution of the relaxation time. For SMM with only one relaxing object  $\alpha$  is close to zero. The extended Debye model was applied to fit simultaneously the experimental variations of  $\chi_M'$  and  $\chi_M''$  with the frequency  $\nu$  of the oscillating field ( $\omega = 2\pi\nu$ ). Typically, only the temperatures for which a maximum on the  $\chi_M''$  vs.  $\nu$  curves, have been considered (see Figure S4 for an example). The best fitted parameters  $\tau$ ,  $\alpha$ ,  $\chi_T$ ,  $\chi_S$  are listed in tables hereunder with the coefficient of determination  $R^2$ .

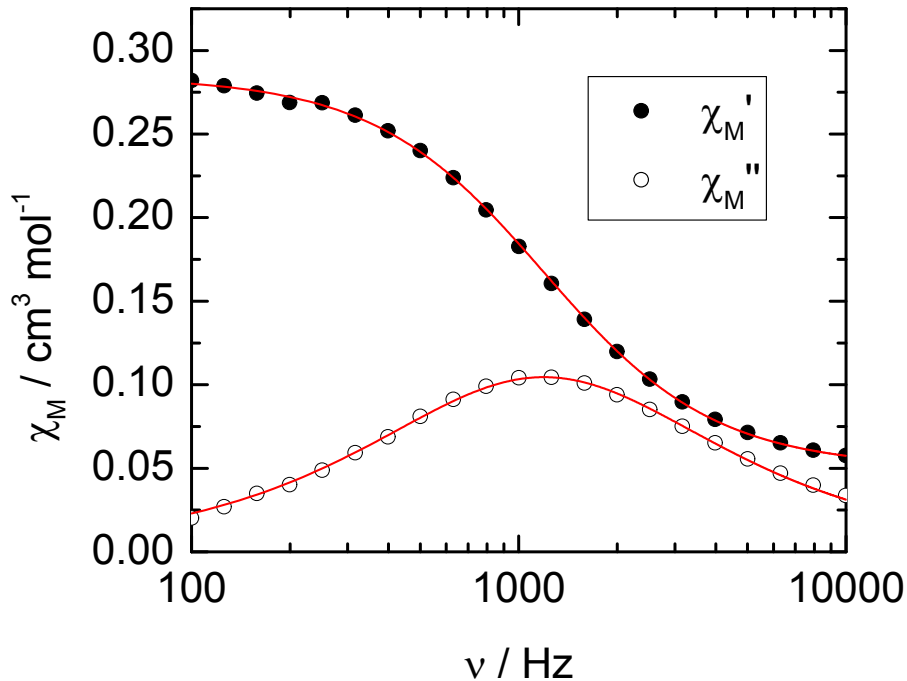


**Figure S4.** Frequency dependence of the in-phase ( $\chi_M'$ ) and out-of-phase ( $\chi_M''$ ) components of the ac susceptibility of  $[\text{Yb}(\mathbf{S},\mathbf{S})\text{-L}_3](\text{OTf})_3$  measured on powder at 2 K at 1 kOe with the best fitted curves (full lines).

**Table S2.** Best fitted parameters ( $\chi_T$ ,  $\chi_S$ ,  $\tau$  and  $\alpha$ ) with the extended Debye model for [Yb(S,S)-L<sub>3</sub>](OTf)<sub>3</sub> at 1 kOe between 2 and 3.5 K.

T / K	$\chi_S / \text{cm}^3 \text{mol}^{-1}$	$\chi_T / \text{cm}^3 \text{mol}^{-1}$	$\alpha$	$\tau / \text{s}$	R <sup>2</sup>
2	0.28531	0.04925	0.07707	1.33431E-4	0.99979
2.2	0.26163	0.04713	0.0711	9.88464E-5	0.9998
2.4	0.24133	0.04525	0.06446	7.29224E-5	0.99974
2.6	0.22456	0.04318	0.06029	5.38149E-5	0.99981
2.8	0.20923	0.04263	0.04816	3.97464E-5	0.99958
3	0.19653	0.04214	0.03869	2.96476E-5	0.99978
3.5	0.17319	0.03528	0.06241	1.40309E-5	0.99866

#### 4) Photophysics and chiroptics

**Absorption:** Absorption spectra were recorded on a JASCO V-650 spectrophotometer in diluted solution (ca.  $10^{-5}$  or  $10^{-6}$  mol L<sup>-1</sup>), using spectrophotometric grade solvents.

**Luminescence:** The luminescence spectra were measured using a Horiba-Jobin Yvon Fluorolog-3 spectrofluorimeter, equipped with a three slit double grating excitation and emission monochromator with dispersions of 2.1 nm/mm (1200 grooves/mm). The steady-state luminescence was excited by unpolarized light from a 450 W xenon CW lamp and detected at an angle of 90°. Spectra were reference corrected for both the excitation source light intensity variation (lamp and grating) and the emission spectral response (detector and grating). Near infra-red spectra were recorded using a liquid nitrogen cooled, solid indium/gallium/arsenic detector (850- 1600 nm) and a RG830 filter to cut any visible emission.

For luminescence lifetimes, the sample was excited using a pulsed Nd:YAG laser (SpectraPhysics), operating at 10 Hz. Light emitted at right angles to the excitation beam was focused onto the slits of a monochromator (PTI120), which was used to select the appropriate wavelength. The growth and decay of the luminescence at selected wavelengths was detected using a Ge photodiode (Edinburgh Instruments, EI-P) and recorded using a digital oscilloscope (Tektronix TDS320) before being transferred for analysis. Luminescence lifetimes were obtained by iterative reconvolution of the detector response (obtained by using a scatterer) with exponential components for growth and decay of the metal-centred luminescence.

##### **Chiroptical measurements:**

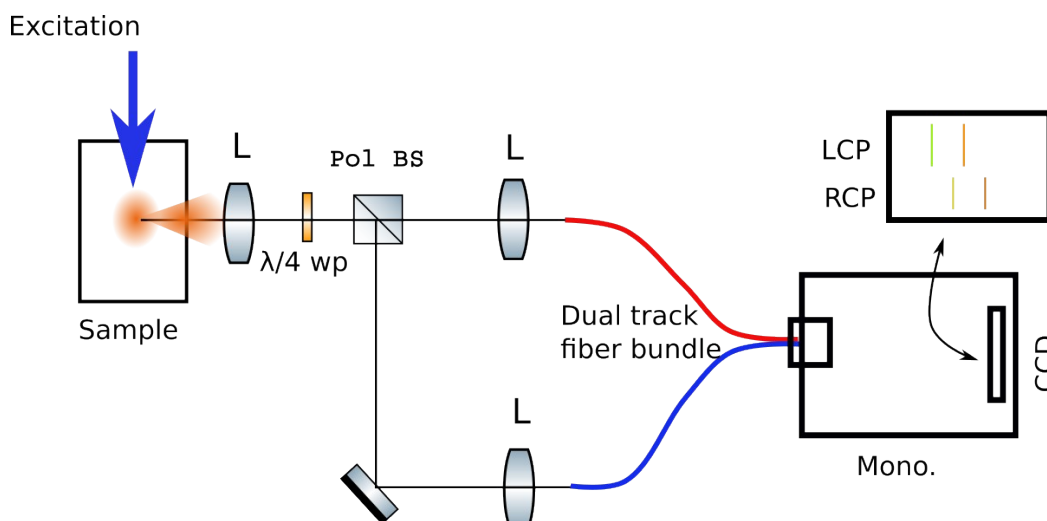
The ECD spectra of ligand **L** and the relative complexes were recorded on a Jasco J710 spectropolarimeter in 0.02 cm quartz cell (4 accumulations) on  $10^{-4}$  M methanol solution for the overall spectrum; for the 250-450 nm window, a 0.05 mm cell was used. NIR-CD spectra were recorded with a Jasco J200 spectropolarimeter on a 4 mM methanol solution in a 1 cm cell (slit-width 3 nm, integration time 4 s., 4 accumulations).

IR and VCD spectra of the complexes of both the enantiomers of ligand **L** (3 mM in deuterated methanol) have been acquired were acquired with a JASCO FVS-4000 instrument using a 100  $\mu$ m KBr cell and were baseline subtracted with the spectra of the cell filled with blank solvent using the same acquisition parameters and recorded immediately after and/or immediately

before the sample. In all cases 6000 or 8000 scans were accumulated for the Ln complexes with a background (50 accumulations) – blank solvent (2000 accumulations) – sample (6000 / 8000 accumulations) methodology.

**NIR CPL set-up.** NIR CPL spectra are recorded on a homemade apparatus displayed in Scheme S2. Solutions in quartz cuvette are excited by UV light from laser diode. The fluorescence is collected with a lens and separated by means of a  $\lambda/4$  waveplate ( $45^\circ$ ) and a polarizing beam splitter. With this arrangement, the light is split into two components of either left- or right-circularly polarized light. Each arm is further imaged on one side of a fiber bundle. The other extremity of the bundle is focused at the entrance slit of a monochromator. The light spectrally separated is imaged on a CCD camera. The “upper/lower” part of the camera record the left- or right-handed circularly polarized spectra. Because of the brightness of the molecules as well as their high glum, this set-up allows a fast record of the CPL spectra in less than one second. However, the silicon detector cut-off prevents for recording at wavelengths longer than 1050 nm.

We also used standard set-up using the PEM/locking detection scheme with an IR photo-multiplier or Si detector for CPL and ECD measurements, respectively. These set-ups are described earlier for helicenes likes CPL measurements<sup>2</sup> and ECD thin film characterization.<sup>3</sup>



Scheme **S2**. Schematic of the NIR-CPL (BS+CCD) based setup. L: lenses;  $\lambda/4$  wp:  $\lambda/4$  waveplates; BS: polarizer beam splitter; Mono: monochromator.

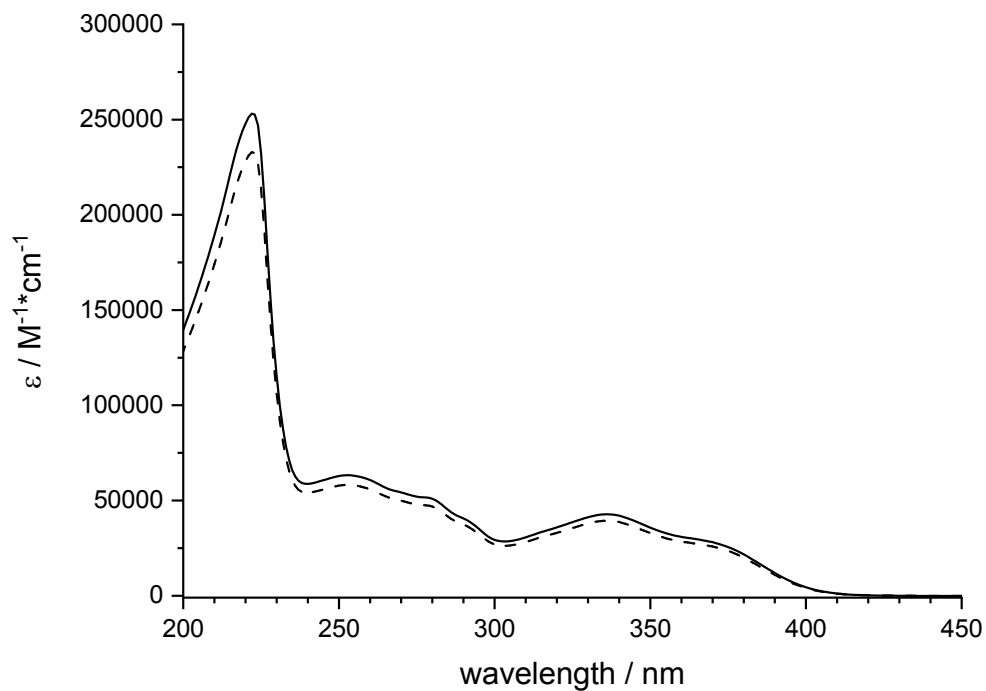


**Figure S5.** Absorption spectra of  $[\text{Yb}(\text{S,S})\text{-L}_3](\text{OTf})_3$  (dotted line) and  $[\text{Yb}(\text{R,R})\text{-L}_3](\text{OTf})_3$  (full line) complexes in methanol solution.

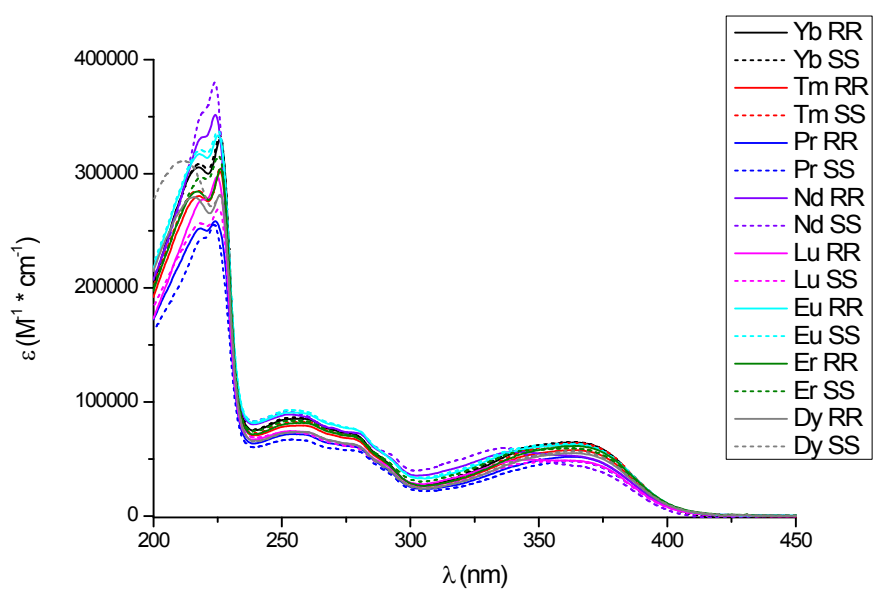


**Figure S6.** Absorption spectra of all other  $[\text{Ln}(\mathbf{S},\mathbf{S})\text{-L}_3](\text{OTf})_3$  and  $[\text{Ln}(\mathbf{R},\mathbf{R})\text{-L}_3](\text{OTf})_3$  complexes involved in this study (Ln = Yb, Tm, Pr, Nd, Lu, Eu, Er, Dy) in methanol solution.

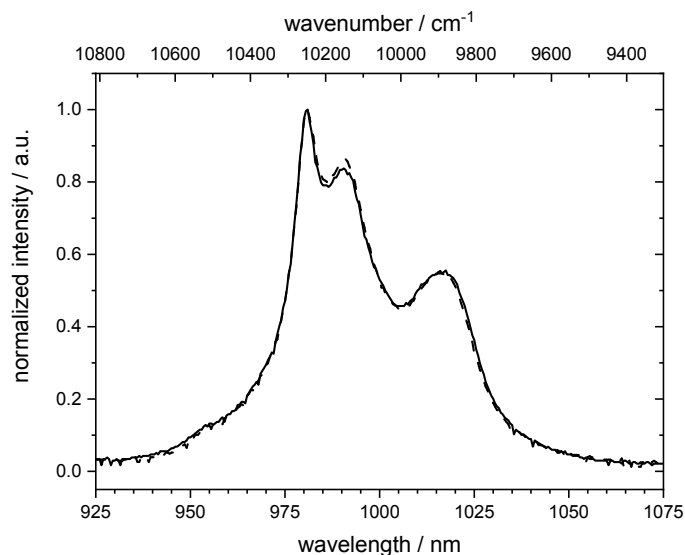


**Figure S7.** Luminescence spectra of  $[\text{Yb}(\mathbf{S},\mathbf{S})\text{-L}_3](\text{OTf})_3$  and  $[\text{Yb}(\mathbf{R},\mathbf{R})\text{-L}_3](\text{OTf})_3$  in solid state at 298 K.

Peak	Solid 77K			Solution 77K		
	position (nm)	position (cm <sup>-1</sup> )	splitting (cm <sup>-1</sup> )	position (nm)	position (cm <sup>-1</sup> )	splitting (cm <sup>-1</sup> )
1	<b>979.2</b>	10212.5	—	<b>980.6</b>	10198.4	—
2	<b>989.8</b>	10103.2	109.4	<b>990.9</b>	10091.6	106.7
3	<b>998.2</b>	10018.1	194.4	<b>1000.3</b>	9997.1	201.3
4	<b>1013.7</b>	9864.9	347.6	<b>1015.9</b>	9843.8	354.6

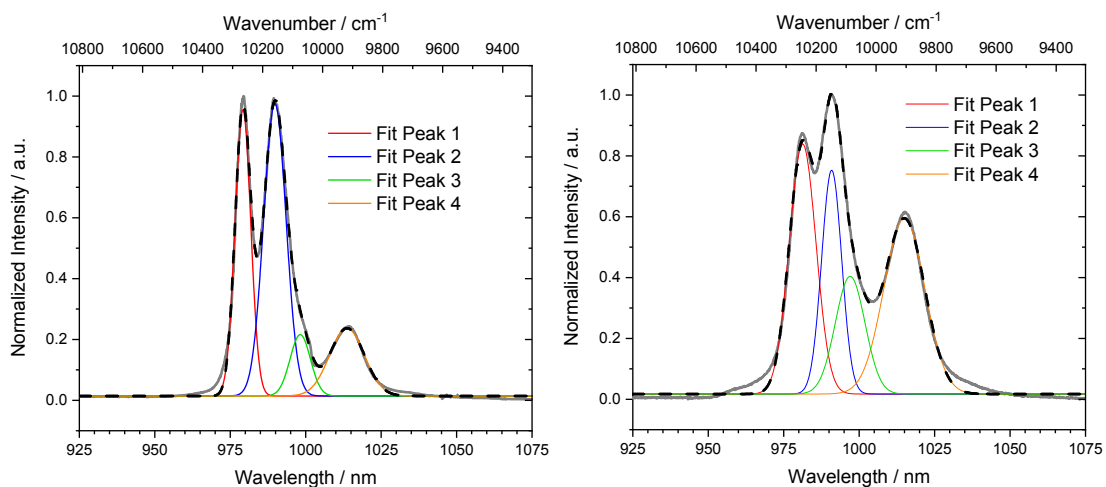


**Figure S8.** Gaussian deconvolution the 77K luminescence spectra of  $[\text{Yb}(\mathbf{S},\mathbf{S})\text{-L}_3](\text{OTf})_3$  complex in solid state (left) and in frozen solution of ethanol : methanol = 4 : 1 (right). The cumulative fittings are depicted as black dashes and the measurements as solid grey lines.

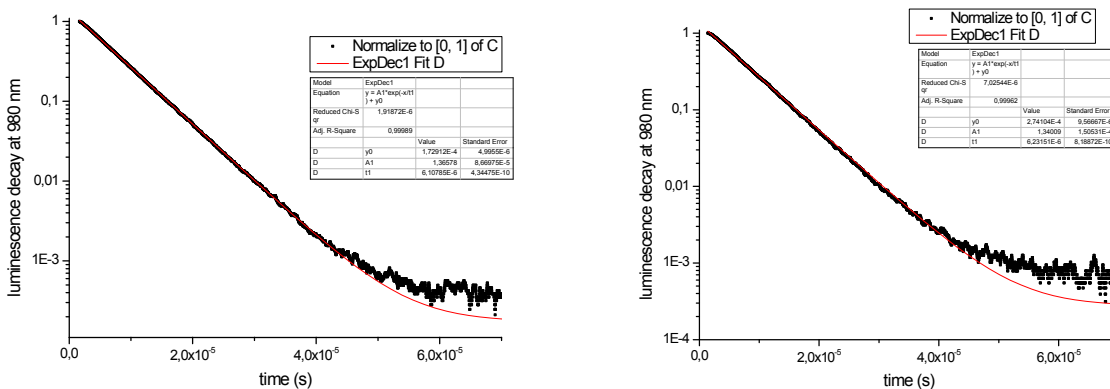


**Figure S9.** Luminescence decay (black) and best monoexponential fit (red curve) in log scale of  $[\text{Yb}(\mathbf{S},\mathbf{S})\text{-L}_3](\text{OTf})_3$  (left) and  $[\text{Yb}(\mathbf{R},\mathbf{R})\text{-L}_3](\text{OTf})_3$  (right) complexes in methanol solution.

### Details of the Boltzmann distribution calculation

The four CF states ( $N_{0-4}$ ) of the  ${}^2F_{7/2}$  ground state of Yb(III) undergo thermal equilibrium and their relative population follows a Boltzmann distribution given as:

$$\frac{N_i}{N_{tot}} = e^{-\frac{E_i}{k_B T}}$$

Consequently, it is possible to estimate this distribution vs temperature by solving the following four-equations system where  $k_B$  represents the Boltzmann constant ( $k_B = 1.38 \cdot 10^{-23} \text{ J}\cdot\text{K}^{-1}$ ),  $E_i$  ( $i = 0-3$ ) the energy of the  $M_j$  states.

$$\left\{ \begin{array}{l} \frac{N_1}{N_0} = e^{-\frac{E_0 - E_1}{k_B T}} \\ \frac{N_2}{N_0} = e^{-\frac{E_0 - E_2}{k_B T}} \\ \frac{N_3}{N_0} = e^{-\frac{E_0 - E_3}{k_B T}} \\ N_0 + N_1 + N_2 + N_3 = N_{tot} \end{array} \right.$$

Thus, the probability of the state  $i$  ( $i = 0-3$ ) is:

$$\frac{N_i}{N_{tot}} = \frac{N_i/N_0}{\sum_{i=0}^3 \frac{N_i}{N_0}} = \frac{e^{-\frac{E_0 - E_i}{k_B T}}}{\sum_{i=0}^3 e^{-\frac{E_0 - E_i}{k_B T}}}$$

Consequently, it is possible to obtain the relative population of each CF excited state vs.  $T$  by knowing the energy diagram obtained from 77K solution luminescence with  $E_1 - E_0 = 106.7 \text{ cm}^{-1}$ ,  $E_2 - E_0 = 201.3 \text{ cm}^{-1}$ ,  $E_3 - E_0 = 354.6 \text{ cm}^{-1}$ . Figure S10 (left) shows the relative population of the ground state with the temperature.

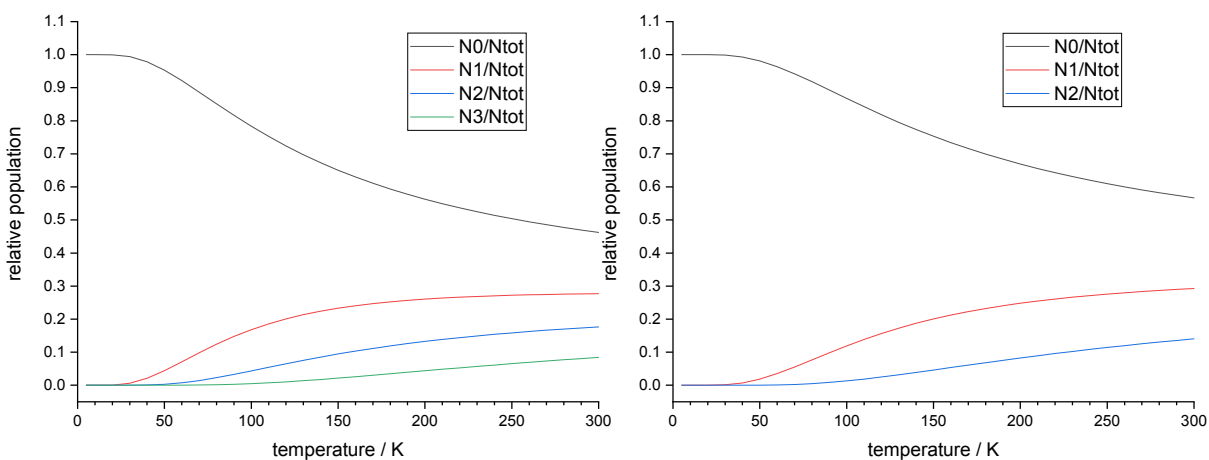


**Figure S10.** Variation of the relative population of the ground (left) and excited (right) CF states with the temperature according to Boltzmann's statistics.

It is also possible to perform the exact same procedure for the  ${}^2F_{5/2}$  lowest emissive excited state that splits in three  $M_J$  states ( $N_{0-2}$ ). In this case, we use only a three-equations system that can be solved in the same way. Thus, the probability of the state  $i$  ( $i = 0-2$ ) is:

$$\frac{N_i}{N_{tot}} = \frac{N_i/N_0}{\sum_{i=0}^2 \frac{N_i}{N_0}} = \frac{e^{-\frac{E_0 - E_i}{k_B T}}}{\sum_{i=0}^2 e^{-\frac{E_0 - E_i}{k_B T}}}$$

Consequently, it is possible to obtain the relative population of each CF excited state vs. T by using the energy diagram obtained from the absorption measurements at RT with  $E_1 - E_0 = 138 \text{ cm}^{-1}$ ,  $E_2 - E_0 = 291 \text{ cm}^{-1}$ . Figure S10 (right) shows the relative population of the excited state with the temperature.

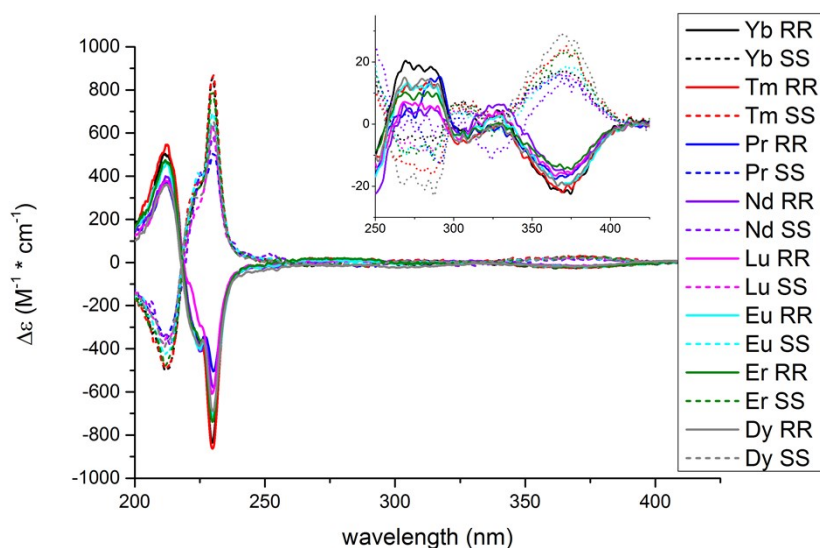


**Figure S11.** Visible ECD spectra of all  $[\text{Ln}(\mathbf{S},\mathbf{S})\text{-L}_3](\text{OTf})_3$  and  $[\text{Ln}(\mathbf{R},\mathbf{R})\text{-L}_3](\text{OTf})_3$  complexes involved in this study (Ln = Yb, Tm, Pr, Nd, Lu, Eu, Er, Dy).

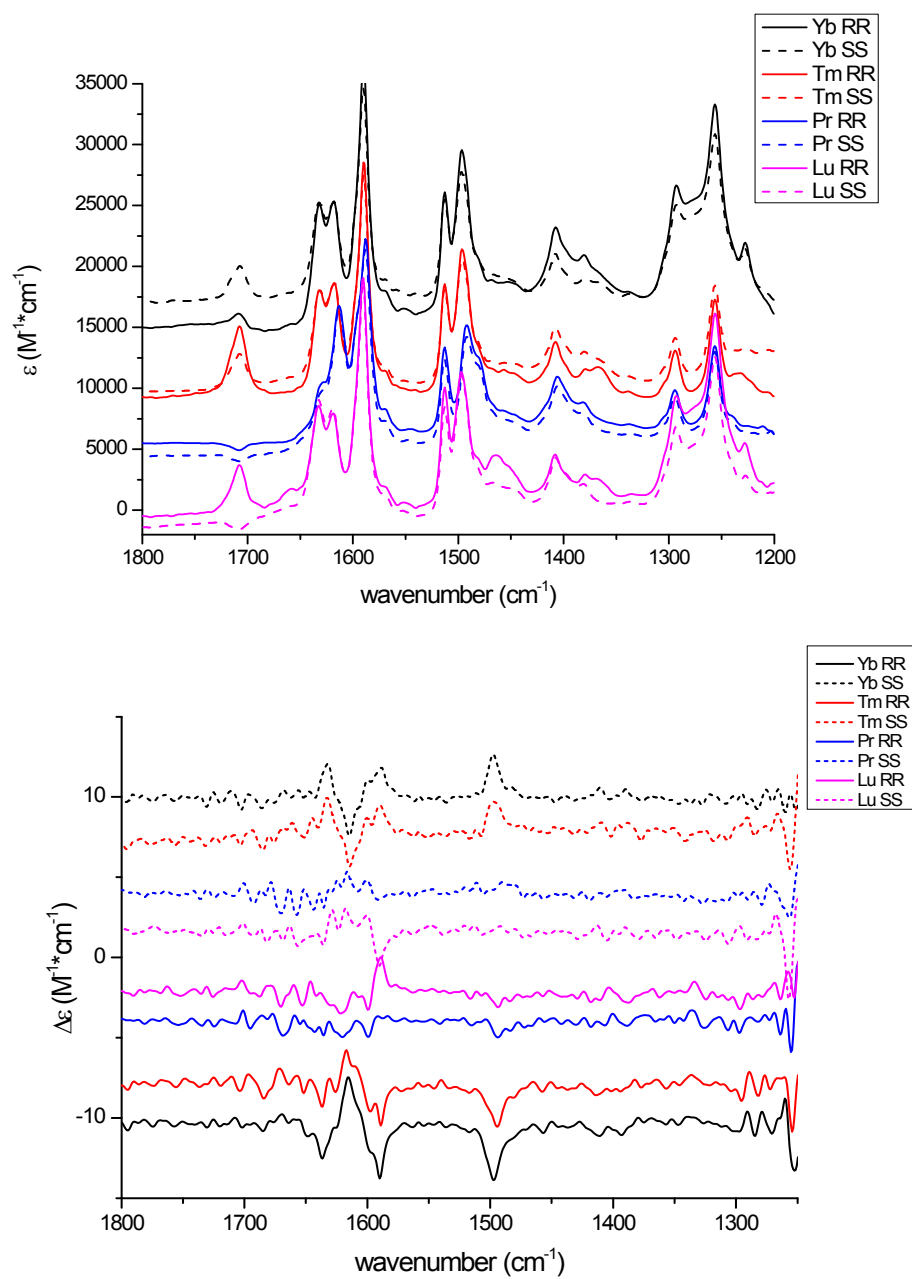


**Figure S12.** FTIR (top) and VCD (bottom) spectra in deuterated methanol at r.t. of all  $[\text{Ln}(\mathbf{S,S})\text{-L}_3](\text{OTf})_3$  and  $[\text{Ln}(\mathbf{R,R})\text{-L}_3](\text{OTf})_3$  complexes involved in this study (Ln = Yb, Tm, Pr, Lu).

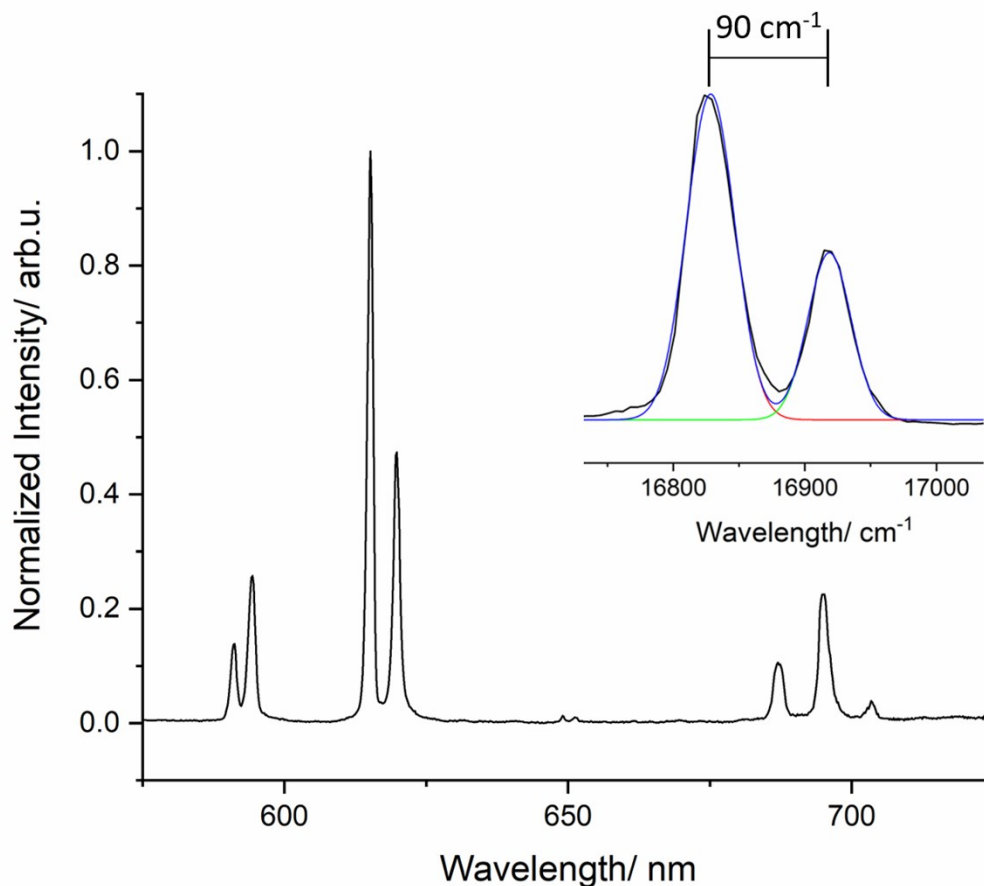


**Figure S13.** Luminescence spectra of  $[\text{Eu}(\mathbf{S,S})\text{-L}_3](\text{OTf})_3$  in solution of EtOH:MeOH = 4:1 at 77 K. In insert is magnified the  $J = 1$  transition illustrating the CF Splitting of  $90 \text{ cm}^{-1}$ .

## 5) Computational details

The multi-reference calculations were carried out with the OpenMolcas software package.<sup>4</sup> The static correlation was treated using the complete active space self-consistent field (CASSCF) approach,<sup>5</sup> while the dynamic correlation was introduced using perturbation theory at the second order (CASPT2).<sup>6</sup> For the CASPT2 calculations, an imaginary shift of 0.25 was used in order to avoid the presence of intruder states in the wave-function. The scalar relativistic (SR) effects were considered with the second-order Douglas-Kroll-Hess<sup>7,8,9,10</sup> SR Hamiltonian in combination with the all-electron atomic natural orbital relativistically contracted (ANO-RCC) basis set from the Molcas library.<sup>11</sup> The following contractions were used for Yb [25s22p15d11f4g2h/8s7p4d3f2g], O and N [14s9p4d3f2g/4s3p2d], C [14s9p4d3f2g/3s2p1d], and H [8s4p3d1f/2s]. For the electronic structure and magnetic properties calculations, the

active space used corresponds to 13 electrons spanning the seven 4f orbitals of the Yb(III) ion. For the CPL calculations, the CAS(13,7) active space was then augmented with the five vacant 5d orbitals of the Yb(III) ion. To do so, the additional 5d orbitals were first optimized within a RAS3 space by allowing single excitations at the RASSCF level, giving the following RAS[13,0,1,0,7,5] space. Using the optimized orbitals, double excitations from the RAS2 space constituted of the 4f orbitals were added at the RASCI level (RAS[13,0,2,0,7,5]). Using this RAS space, dynamic correlation were added at the PT2 level with a real shift of 0.65 to avoid intruder states. Such a procedure was used in a previous work to calculate the CPL of an analogous Eu(III) complex.<sup>12</sup> In order to describe the low-lying 4f states, the state-average formalism was used with 7 SR spin-doublet states. The spin-orbit coupling was then introduced within a state interaction among the basis of the calculated SR spin-doublets using the restricted active space state interaction (RASSI) approach.<sup>13</sup> In these SO calculations, either the SR CASSCF or the SR CASPT2 energies were used to construct the SOC matrix. The resulting magnetic properties, namely the EPR g-factor, the magnetic susceptibility, the magnetization and the ab-initio crystal-field parameters were calculated using the RASSI and Single\_Aniso modules of OpenMolcas.<sup>14</sup> Finally, the nature of the SO ground state was analyzed using natural spin orbitals as implemented in the RASSI module.<sup>15</sup> These orbitals were then visualized with the graphical interface of the ADF software package. The simulated CPL spectra were obtained as the sums of Gaussian functions (with the root mean square width of  $\sigma = 0.005$  eV) centered at the vertical excitation energies.

The ab-initio calculations were performed on an idealized model structure of  $[\text{YbL}'_3]^{3+}$  derived from the NMR structure. For this model compound, positions of the hydrogen atoms were optimized using Kohn-Sham density functional theory (KS-DFT) and the Gaussian 09 software package.<sup>16</sup> The structure optimization employed the hybrid functional B3LYP.<sup>17</sup> Here, the second-order Douglas-Kroll-Hess SR Hamiltonian was used in combination with a 28-electron quasi-relativistic effective core potential (ECP) for ytterbium with a matching ECP28MWB-SEG valence basis, whereas a double- $\zeta$  polarized Gaussian-type orbital basis sets with polarization were used for the ligand atoms.

**Table S3.** Relative energies (in  $\text{cm}^{-1}$ ) and electronic g-factors for the ground and excited Kramers doublet states of the model compound  $[\text{YbL}'_3]^{3+}$  obtained at the SCF-SO and PT2-SO level with the CAS(13,7) active space.

	SCF-SO			PT2-SO		
	$\Delta E$	$g_{\parallel}$	$g_{\perp}$	$\Delta E$	$g_{\parallel}$	$g_{\perp}$
${}^2F_{7/2}$	0	3.46	1.33/0.98	0	3.38	1.93/0.57
	53	3.34	0.59/0.23	86	3.38	0.83/0.06
	79	5.67	2.29/1.47	138	5.54	2.53/1.34
	177	1.04	3.96/3.85	290	1.03	3.94/3.86
${}^2F_{5/2}$	10331			10356		
	10341			10385		
	10429			10522		

**Table S4.** Composition (in per-cent) of the calculated ground state in term of the total angular momentum J and of its projections  $M_J$  for the model compound  $[\text{YbL}'_3]^{3+}$ .

GS composition in term of $ 7/2, \pm M_J\rangle$	
SCF-SO	67 $ 7/2, \pm 5/2\rangle$ + 13 $ 7/2, \mp 7/2\rangle$ + 7 $ 7/2, \mp 3/2\rangle$ + 7 $ 7/2, \mp 1/2\rangle$
PT2-SO	63 $ 7/2, \pm 5/2\rangle$ + 17 $ 7/2, \mp 7/2\rangle$ + 11 $ 7/2, \mp 3/2\rangle$ + 8 $ 7/2, \mp 1/2\rangle$

**Table S5.** Energy ( $\Delta E$  in eV), rotatory strength (R in  $10^{-40}$  esu  $\text{cm}^2$ ) and CPL intensity ( $\Delta I$ ) calculated at the RASPT2 level for each CPL transitions at 0K.

Transitions	$\Delta E$	R ( $\times 10^{40}$ )	$\Delta I$
$0' \rightarrow 0$	1.34306	1.67E-1	5.75E-5
$0' \rightarrow 1$	1.32784	-8.11E-2	-2.66E-5
$0' \rightarrow 2$	1.32141	-2.73E-3	-8.78E-7
$0' \rightarrow 3$	1.29571	-1.53E-2	-4.55E-6

$1' \rightarrow 0$	1.35413	3.91E-1	1.39E-4
$1' \rightarrow 1$	1.33891	-1.51E-1	-5.12E-5
$1' \rightarrow 2$	1.33248	-2.73E-1	-9.09E-5
$1' \rightarrow 3$	1.30678	1.54E-1	4.74E-5
$2' \rightarrow 0$	1.37751	-2.35E-1	-8.91E-5
$2' \rightarrow 1$	1.36229	7.90E-2	2.87E-5
$2' \rightarrow 2$	1.35586	1.17E-1	4.16E-5
$2' \rightarrow 3$	1.33016	-1.57E-1	-5.19E-5

At T = 300K, the calculated Boltzmann populations gave 52, 34 and 14 % for 0', 1' and 2', respectively.

**Table S6.** Ab-initio CF parameters (in  $\text{cm}^{-1}$ ) calculated for  $[\text{YbL}'_3]^{3+}$  at the PT2-SO level.

B2-2	8.757
B2-1	-4.086
B20	-23.758
B21	2.107
B22	-10.327
B4-4	-29.981
B4-3	-15.704
B4-2	-36.477
B4-1	-44.741
B40	-46.750
B41	-1.560
B42	22.060
B43	-79.994
B44	-5.887
B6-6	-24.979
B6-5	-22.572
B6-4	-18.615
B6-3	-5.955
B6-2	-29.108
B6-1	-14.726
B60	-10.882
B61	1.874
B62	18.124
B63	-29.600
B64	-0.800

---

B65	23.541
B66	-56.689

---

## 6) Paramagnetic NMR Analysis and solution structure calculation

The Ytterbium complex solution structure has been calculated with the FORTRAN routine PERSEUS, which requires a starting structural model and the PCS (pseudocontact shifts) values of proton and carbon resonances of the Yb derivative as two main inputs. The extraction of these values requires a detailed NMR assignment of the different paramagnetic derivatives and a diamagnetic one (Lutetium in our case).

The  $^1\text{H}$  and  $^{13}\text{C}$ -NMR spectra of the complete series  $[\text{LnL}_3](\text{OTf})_3$  ( $\text{Ln} = \text{Nd}, \text{Pr}, \text{Eu}, \text{Dy}, \text{Tm}, \text{Er}, \text{Yb}$ ) have been recorded in deuterated methanol:  $[\text{Yb}(\mathbf{R,R})\text{-L}_3](\text{OTf})_3$ .  $^1\text{H}$ -NMR spectrum is characterized by one set of 13 narrow resonances (the amide NH protons cannot be observed owing to H/D exchange), which highlights the  $D_3$  symmetry of the system. All the complexes appeared to be remarkably stable in methanol solution considering that after several months the NMR samples did not show any sign of alteration/degradation. The assignment of proton and carbon resonances of the diamagnetic  $[\text{LuL}_3](\text{OTf})_3$  complex was straightforward, done with common 1D- and 2D-NMR sequences, while for the paramagnetic derivatives  $[\text{LnL}_3](\text{OTf})_3$  a more hybrid approach is usually required.

The assignment for the different lanthanide complexes usually varies from ion to ion, because is intimately connected to the particular fast longitudinal relaxation and the large linewidths which can limit the possibility of using certain 2D sequences. Interestingly, both Pr and Yb complexes possess average  $T_1$  values long enough to get an almost complete  $^1\text{H}/^{13}\text{C}$  picture of the system. A starting structural model has been built as one unique ligand unit, considering the  $D_3$  symmetry, from the XRD structure of the 4-not substituted Tb complex reported by Gunnlaugsson in 2007, modified *ad hoc* as the  $(\mathbf{R,R})\text{-L}$  ligand bearing an  $\text{Yb}^{3+}$  ion (Figure S14). This model seemed to be a good starting point for the study of the  $\mathbf{L}$  system, either as a guide for the NMR assignment (for a nucleus in a certain position of space relatively to the paramagnetic ion a certain shift is expected in term of sign and magnitude) and also as the input for the solution structure calculation.

Interestingly, it is possible to “translate” the resonances of an already assigned Ln derivative into a different one using the Bleaney’s constants; these calculated values are useful for the rationalization of all the other paramagnetic complexes resonances.

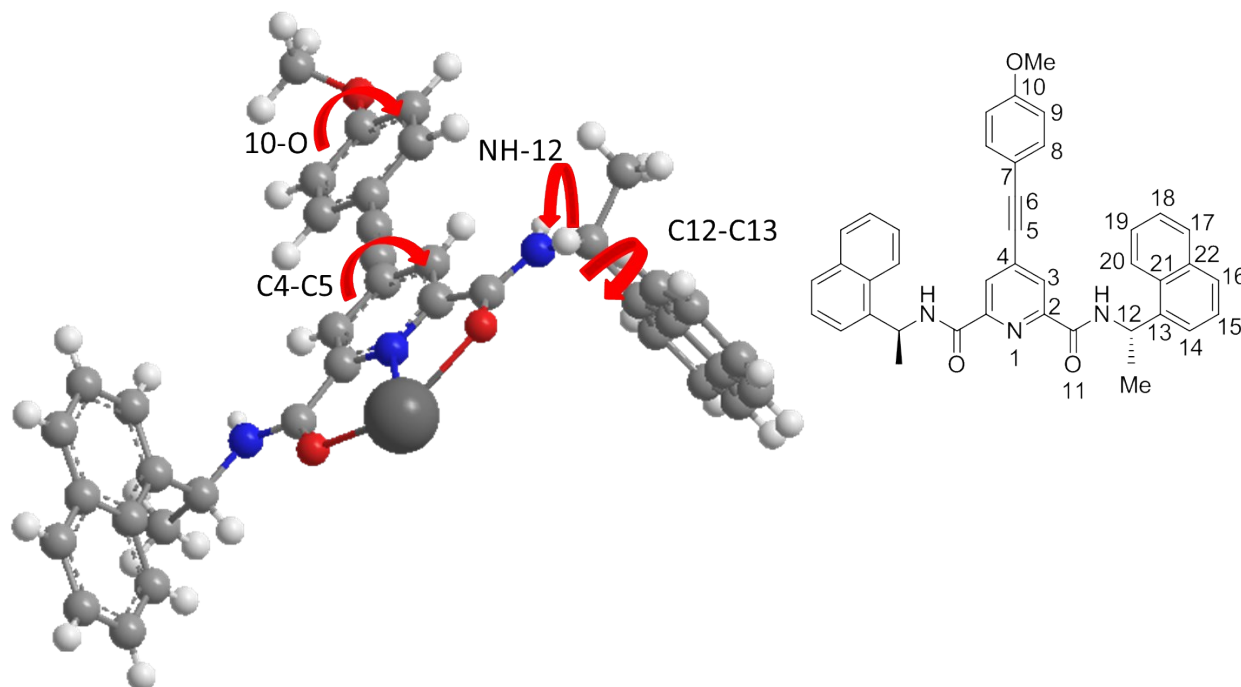


**Figure S14.** Starting structural model (left) and NMR numbering labels (right).

Then, exploiting this model to rationalize the shifts, T1 values, multiplicity, integrals and connectivity with HSQC and HMBC maps, Pr and Yb complexes were fully assigned for both proton and carbon resonances and used as a guide for the assignment of all the other paramagnetic derivatives which is reported in Table S6.

Noteworthy, this starting model lacks of reliability, especially for some important dihedral angles: in Figure S15 is depicted the plot between the proton longitudinal paramagnetic relaxation rates ( $\rho_1^{\text{para}}$ ) vs.  $r^{-6}$  (nucleus distance from the Yb ion in Å taken from the structure). Some nuclei (H14 and H20) lay outside the expected linear trend as an indication that the relative orientation of the naphthyl moiety with respect to the major symmetry axis and then the distances of all these nuclei from the Ln<sup>3+</sup> ion required optimization.

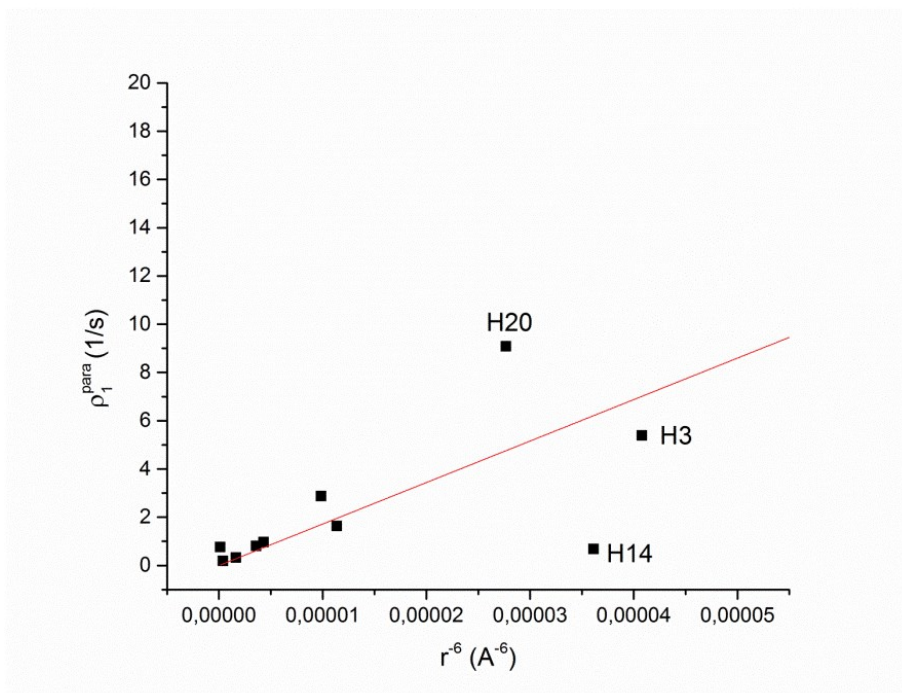


**Figure S15.** Plot of the paramagnetic longitudinal relaxation rates vs. distances taken from the starting model (Figure S14).

The quality of the assignment throughout the lanthanide series has been confirmed considering the excellent linear trend within the plots in Figures S16 and S17 which depict the paramagnetic shifts of all the nuclei of a certain lanthanide versus the Yb derivative. This good trend even for carbon atoms (more affected by the contact contribution) is remarkable and confirms not only the correct assignment, but is also a strong proof of isostructurality of the **L** system along the Ln series. This plot also helps to spot the carbon atoms which most experience the contact contribution (C3 of the pyridine, C14 and C16 of the naphthyl ring) and then their use in the structure calculation step has to be considered carefully.

The extraction of the PCS contribution from the total paramagnetic shifts for the  $[\text{YbL}_3](\text{OTf})_3$  complex has been achieved using the method reported by Di Pietro *et al.* in 2011.<sup>18</sup>

**Table S7.** Assignment of all the lanthanide complexes for the (*R,R*)-L ligand (values in ppm).

H/C	Pr <sup>1</sup> H	Pr <sup>13</sup> C	Nd <sup>1</sup> H	Nd <sup>13</sup> C	Eu <sup>1</sup> H	Eu <sup>13</sup> C	Dy <sup>1</sup> H	Dy <sup>13</sup> C	Er <sup>1</sup> H	Er <sup>13</sup> C	Tm <sup>1</sup> H	Tm <sup>13</sup> C	Yb <sup>1</sup> H	Yb <sup>13</sup> C	Lu <sup>1</sup> H	Lu <sup>13</sup> C
<b>2</b>																
<b>3</b>	10.8	144.02	8.94	145.37	4.16	89.24	32.26		-1.07		-4.71		2.84	112.82	7.02	125.48
<b>4</b>		142.94														144.21
<b>5</b>		90.61		90.66		80.8										87.2
<b>6</b>		101.73		101.87		104.2						97.9		100.2		102.25
<b>7</b>		114.33		114.88		112.4						110.52		112.4		114.14
<b>8</b>	8.64	135.26	8.2	134.79	7.48	135.25	13.8	141.8	6.13	133.76	5.32	132.8	6.96	134.15	7.93	134.92
<b>9</b>	7.6	116.65	7.38	116.46	7.1	115.49	10.5	119.19	6.39	114.77	5.94	114.46	6.78	115.43	7.29	116.04
<b>10</b>		162.25		163.3		163.3						162		162.4		163.39
<b>MeO</b>	4.2	56.17	4.09	55.98	3.89	55.8	5.93	57.79	3.45	55.78	3.18	54.84	3.7	55.62	4	55.95
<b>11</b>																
<b>NH</b>																
<b>12</b>	-0.25	48.407	3.77	49.9	9.48	48.53	-48.6		24.36				15.05		5.57	48.97
<b>Me</b>	0.59	20.18	1.3	20.7	2.13	22.85	-9.29				6.31	26.93	3.3	23.52	1.55	21.35
<b>13</b>		139.9				141.7								140.7		141.08
<b>14</b>	8.72	131.55	7.89	121.57	5.25	118.95	33.98		-1.3		-5.41		2.26	116.33	6.86	120.24
<b>15</b>	9.32	128.2	7.99	126.62	6.26	124.57	25.35		2.01		-0.64	116.66	4.38	122.5	7.35	125.84
<b>16</b>	9.77	123.32	8	128.97	6.75	127.42	20.47		3.8	123.71	1.97	121.5	5.51	126.06	7.58	128.7
<b>17</b>	9	130.23	8.1	131.07	7.3	130.33	15.75	137.94	5.49	128.8	4.44	128.02	6.57	129.98	7.82	131.07
<b>18</b>	7.87	127.18	7.7	126.98	7.53	126.81	9.63	128.72	7.04	126.33	6.84	126.35	7.35	126.74	7.66	126.94
<b>19</b>	6.29	126.35	7.11	126.99	8.25	127.76	-2.63		10.51	129.27	11.95	130.51	9.2	128.63	7.58	127.6
<b>20</b>	3.99	120.6	6.59	121.95	10	123.38	-25.06		17.59		21.82		13.13	124.73	7.87	122.46
<b>21</b>		129.26		130.6		130.1								129.7		130.48
<b>22</b>		133.9		136.3		133.4								132.28		134.26

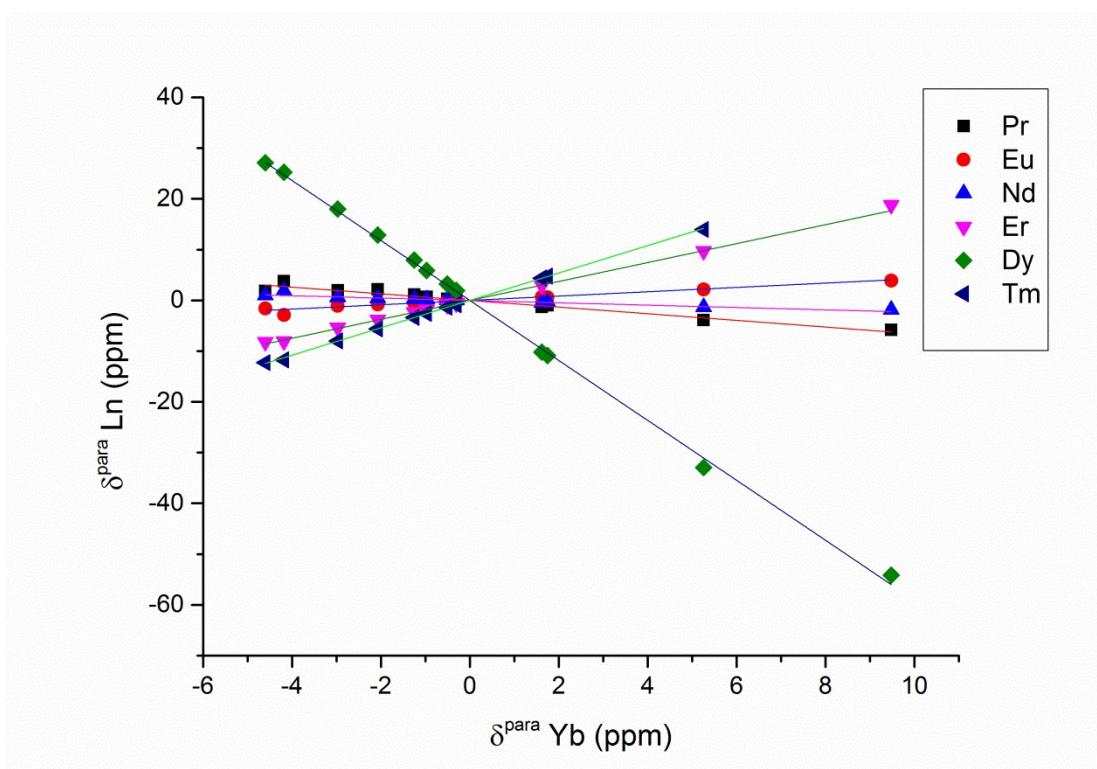


**Figure S16.** Paramagnetic shifts plot for proton resonances with respect to the Yb one.

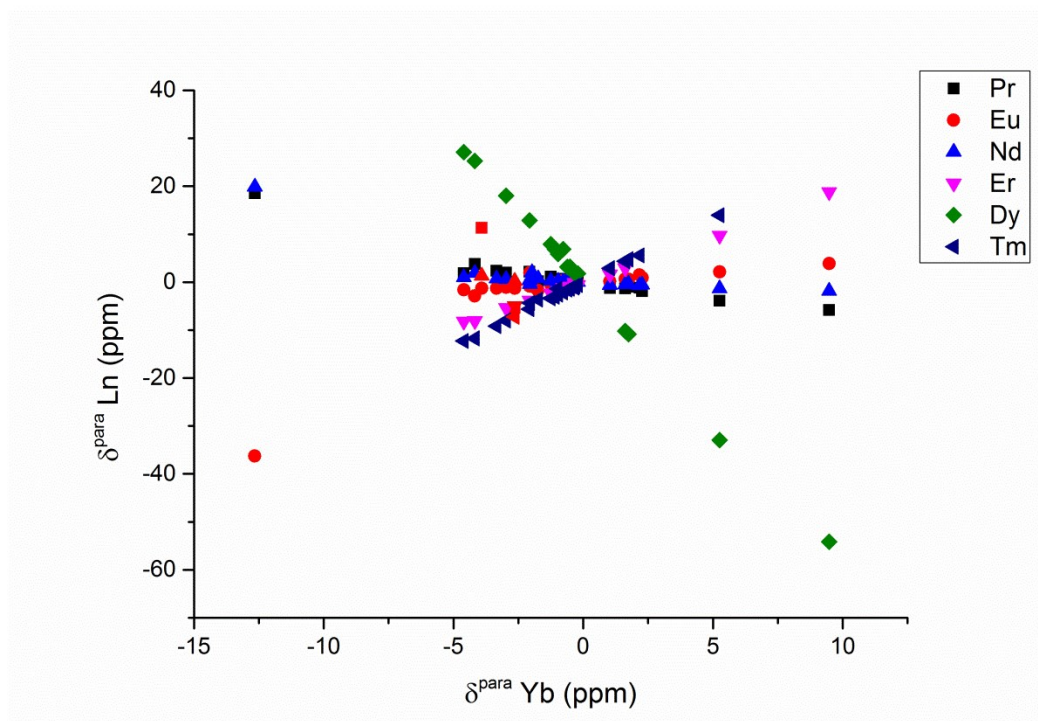


**Figure S17.** Paramagnetic shifts plot for proton and carbon resonances with respect to the Yb one.

This method consists of precise steps:

- 1) From the  $\delta^{\text{para}}_{\text{Ln}}$  vs  $\delta^{\text{para}}_{\text{Yb}}$  plot of Figure S16 the  $m$  slopes are extracted for each Ln/Yb couples (Table S7). Just the proton resonances are considered, because they are more insensitive to the contact contribution.

**Table S8.**  $m$  slopes from plots in Figure S16,  $\langle S_z \rangle$  values from reference 18 and their ratio.

	Yb	Pr	Nd	Eu	Er	Dy	Tm
$m$	1	-0.65504	-0.23172	0.42686	1.911315	-5.90787	2.69811
$\langle S_z \rangle$	-2.59	2.97	4.49	-10.68	-15.37	-28.54	-8.21
$m/\langle S_z \rangle$	-0.3861	-0.22055	-0.05161	-0.03997	-0.12435	0.207003	-0.32864

- 2) The second step consists of a series of plots (modified Reilley's plot, Figure S18 for just proton nuclei and S19 for the carbon ones) which depict a single nucleus (H or C atom) along the series: the ratio  $\delta^{\text{para}}_{\text{Ln}}$  of  $i$ -th nucleus for each Ln /  $\langle S_z \rangle$  versus  $m/\langle S_z \rangle$  ( $m$  and  $\langle S_z \rangle$  are Ln dependent). The linear trend of this plot for each nucleus show how much will be reliable the extraction of its PCS. For some resonances (carbon atoms in particular) we did a post plot elaboration, which consisted in excluding the Pr term which represent the lanthanide that much suffer of contact along the series. The results of these plots and the elaboration for C16, C17 and C21 are reported in the Figures S20 and S21.

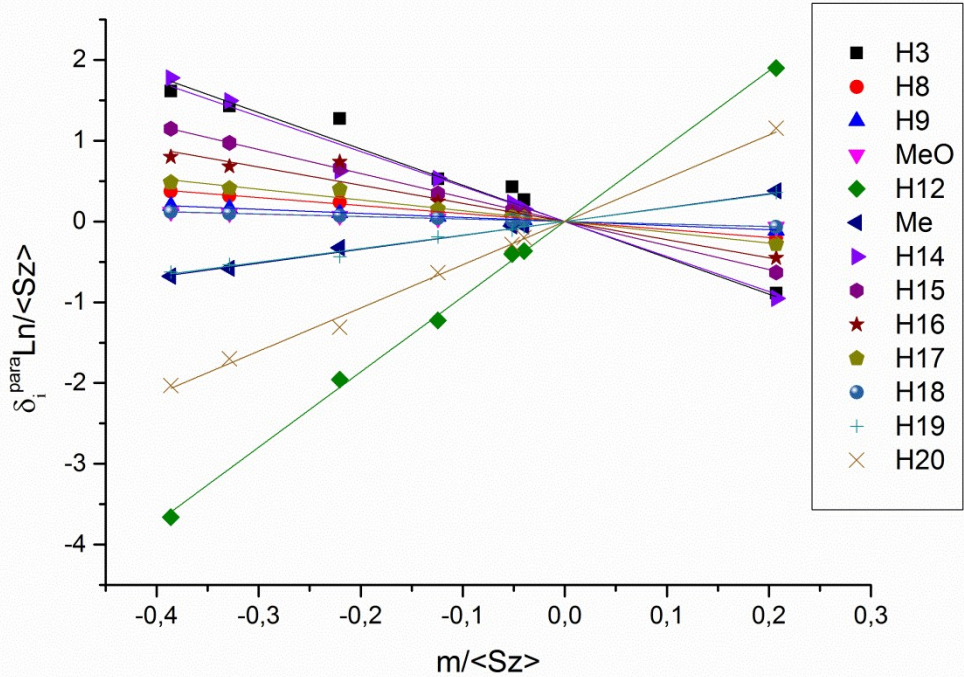


Figure S18. Modified Reilley's plot for all the proton nuclei.

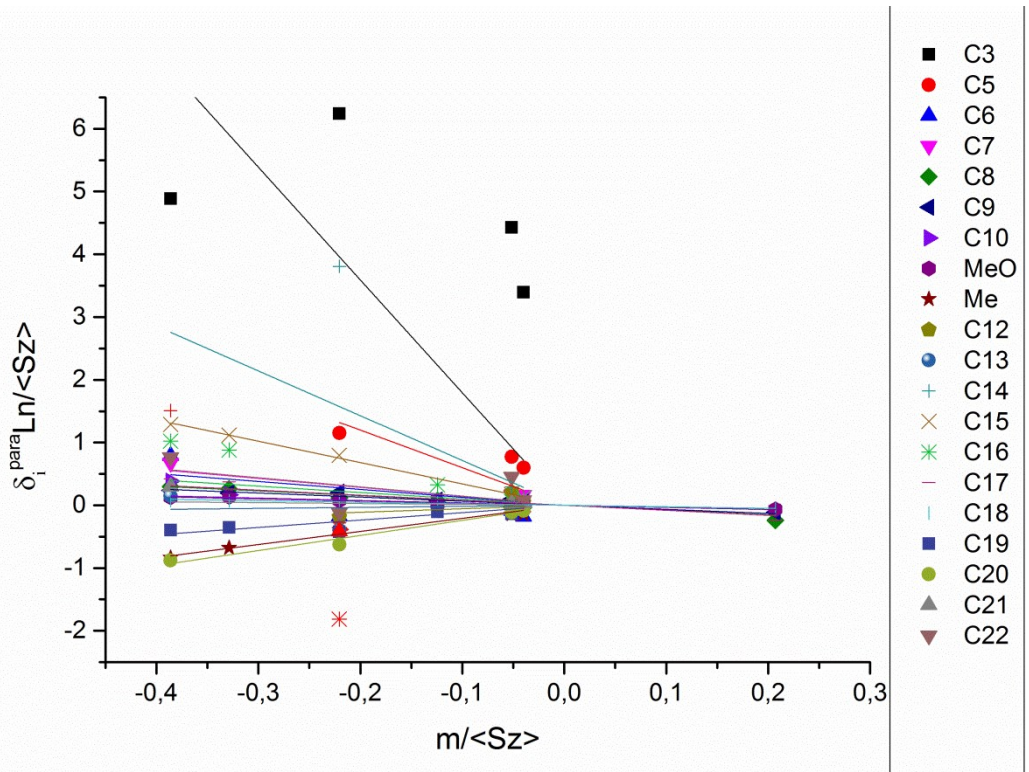
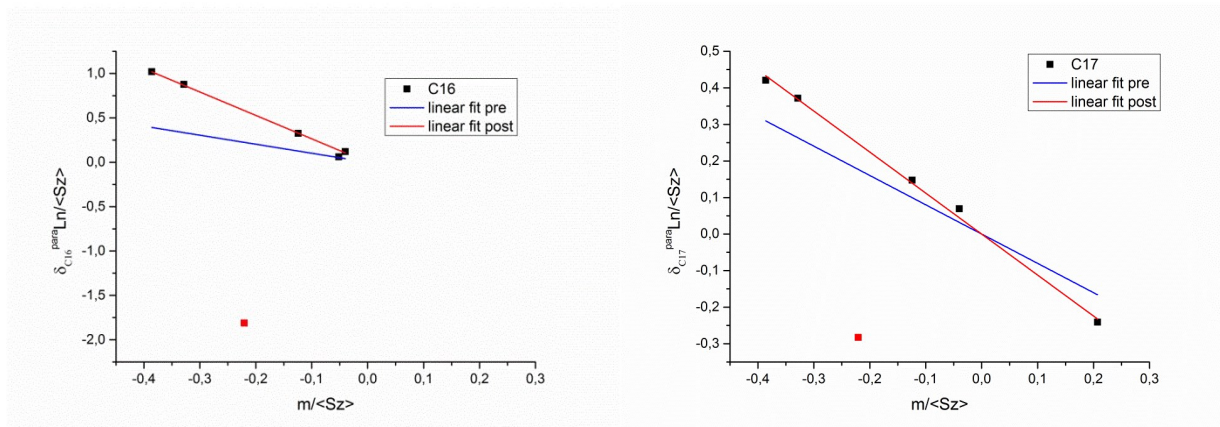
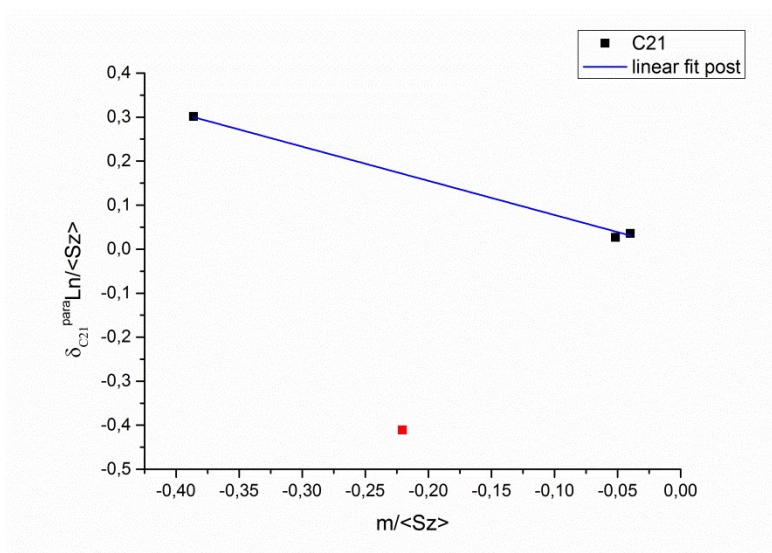


Figure S19. Modified Reilley's plot for all the carbon nuclei.



**Figure S20.** (left) Elaboration for C16 excluding Pr. (right) Elaboration for C17 excluding Pr.



**Figure S21.** Elaboration for C21 excluding Pr.

- 3) From  $\delta_{i,\text{para}} / \langle Sz \rangle$  vs  $m^{\text{Ln}} / \langle Sz \rangle$  plots ( $i$ -th nucleus, Ln is the different lanthanides) a new series of slopes is extracted,  $M$ , which represents the PCS of that nucleus for the Yb derivative. The PCS have been used in the PERSEUS structure optimization (Table S8). In Table S8 are reported the PCS values for proton and carbon atoms before and after a re-elaboration of some carbon resonances.

**Table S9.** H and C PCS (ppm) values for the Yb derivative and the relative R<sup>2</sup> from the plot in Figure S18. For some C PCS a post re-elaboration value is reported with the relative R<sup>2</sup>.

H/C	H PCS	C PCS	R <sup>2</sup> plot	C PCS 2.0	R <sup>2</sup> plot
2					
3	-4.49277	-17.96382	0,59119		
4					
5		-5.99097	0,75408		
6		-1.26410	0,28351		
7		-1.42845	0,74596		
8	-0.9876	-0.76421	0,90677		
9	-0.50339	-0.65026	0,93377		
10		-0.38025	-0,07632		
MeO	-0.3049	-0.34101	0,95561		
11					
NH					
12	9.31899	0,55709	-0,19419		
Me	1.71860	2.08665	0,99072		
13		0.16707	-0,45434		
14	-4.33242	-7.14373	0,48071		
15	-2.97063	-3.40132	0,99901		
16	-2.24761	-1.01556	-0,12273	-2.63738	0.99605
17	-1.33263	-0.8018	0,38805	-1.12163	0.9972
18	-0.31193	-0.2445	0,93335		
19	1.67771	1.17985	0,9063		
20	5.3512	2.40534	0,98632		
21		-0.14101	-0,31285	-0.7766	0.99675
22		-1.46104	0,3746		

Considering the perfect linearity of the modified Reilley's plots for the proton resonances (Figure S18), we gave full credit to these values (green). Moving towards the PCS of the carbon resonances, from the R<sup>2</sup> of the relative plot we divided the results in green, yellow and red, to underline the more or less reliability of the value to be used in the structure optimization step. For C16, C17 and C21 carbon atoms we obtained an improvement of the PCS values excluding the Pr derivative from the plot. We used all the green and the yellow values for the structure calculation of both H and C atoms.

In Figure S14 are reported the main degree of freedom of the structure to be optimized in the starting model which was used as input to the PERSEUS routine together with the extracted PCS and the paramagnetic relaxation rates of the Yb complex.

The main optimization details have been:

- the rotation around C4-C5 bond (or C6-C7) which determines if the phenyl and the pyridine ring are more or less coplanar;
- the whole pyridine bis-amide fragment has to be imposed planar
- the orientation of Me and the naphthyl rings through NH-12 and C12-C13 bond rotation has to be optimized.
- The distances between the Yb and the N1 and the carbonyl oxygen atoms are fixed to 2.5 angstrom and 2.4 angstrom respectively (taken from the XRD structure).
- Finally, the optimization takes into account the symmetry of the ligand fragment.

In the Table S7 are reported the calculated and the experimental values of PCS (ppm) resulting from the successful PERSEUS optimization with the relative difference (Delta).

**Table S10.** Comparison between the PCS values (ppm) calculated by PERSEUS in the optimization of the structure and the experimental extracted ones.

	PCS calc	PCS exp	Delta
	-4.98	-4.49	-0.49
<b>H3</b>	-4.29	-4.49	0.2
	-1.11	-0.99	-0.12
<b>H8</b>	-1.13	-0.99	-0.14
	-0.57	-0.5	-0.07
<b>H9</b>	-0.58	-0.5	-0.08
	-0.3	-0.3	0
	-0.38	-0.3	-0.08
<b>H MeO</b>	-0.39	-0.3	-0.08
	-1.07	-0.76	-0.31
<b>C8</b>	-1.08	-0.76	-0.32
	-0.72	-0.65	-0.07
<b>C9</b>	-0.73	-0.65	-0.08
<b>C MeO</b>	-0.38	-0.34	-0.04
	8.96	9.32	-0.36
<b>H12</b>	9.22	9.32	-0.1
	2.59	2.09	0.5
<b>C Me</b>	2.76	2.09	0.67

	3.63	1.72	1.91
	1.09	1.72	-0.63
	2.43	1.72	0.71
	3.84	1.72	2.12
	1.26	1.72	-0.46
<b>Me</b>	2.48	1.72	0.76
	9.17	12.1	-2.93
<b>H14</b>	9.43	12.1	-2.67
	-2.52	-2.97	0.45
<b>H15</b>	-2.58	-2.97	0.39
	-1.77	-2.25	0.48
<b>H16</b>	-1.86	-2.25	0.39
	-1.1	-1.33	0.23
<b>H17</b>	-1.22	-1.33	0.11
	-0.34	-0.31	-0.03
<b>H18</b>	-0.52	-0.31	-0.21
	1.34	1.68	-0.34
<b>H19</b>	1.09	1.68	-0.59
	4.41	5.35	-0.94
<b>H20</b>	4.19	5.35	-1.16
<b>C9</b>	-1.43	-1.43	0
<b>C8</b>	-2.32	-1.26	-1.06
<b>C12</b>	-0.63	-0.38	-0.25
	-3.19	-7.14	3.95
<b>C14</b>	-3.2	-7.14	3.94
	-2.76	-3.4	0.64
<b>C15</b>	-2.85	-3.4	0.55
	-0.34	-0.24	-0.09
<b>C18</b>	-0.54	-0.24	-0.3
	0.86	1.18	-0.32
<b>C19</b>	0.6	1.18	-0.58
	-2.11	-2.64	0.53
<b>C16</b>	-2.23	-2.64	0.41
	-1.04	-1.12	0.08
<b>C17</b>	-1.22	-1.12	-0.1
	1.89	2.41	-0.52
<b>C20</b>	1.64	2.41	-0.77
	-0.4	-0.78	0.38
<b>C21</b>	-0.58	-0.78	0.2
	-1.52	-1.46	-0.06
<b>C22</b>	-1.7	-1.46	-0.24

---

## 7) NMR spectra

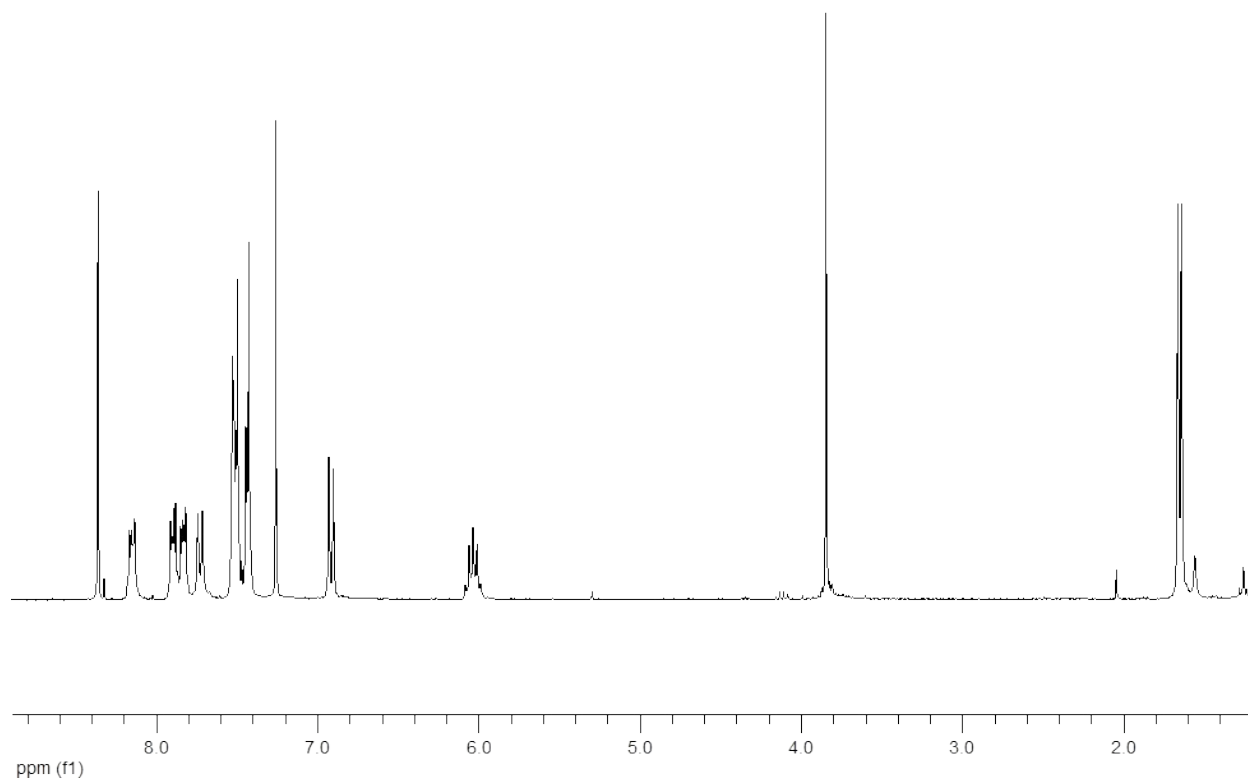


**Figure S21.** <sup>1</sup>H-NMR spectrum (300 MHz, CDCl<sub>3</sub>) of (*R,R*)-L ligand.

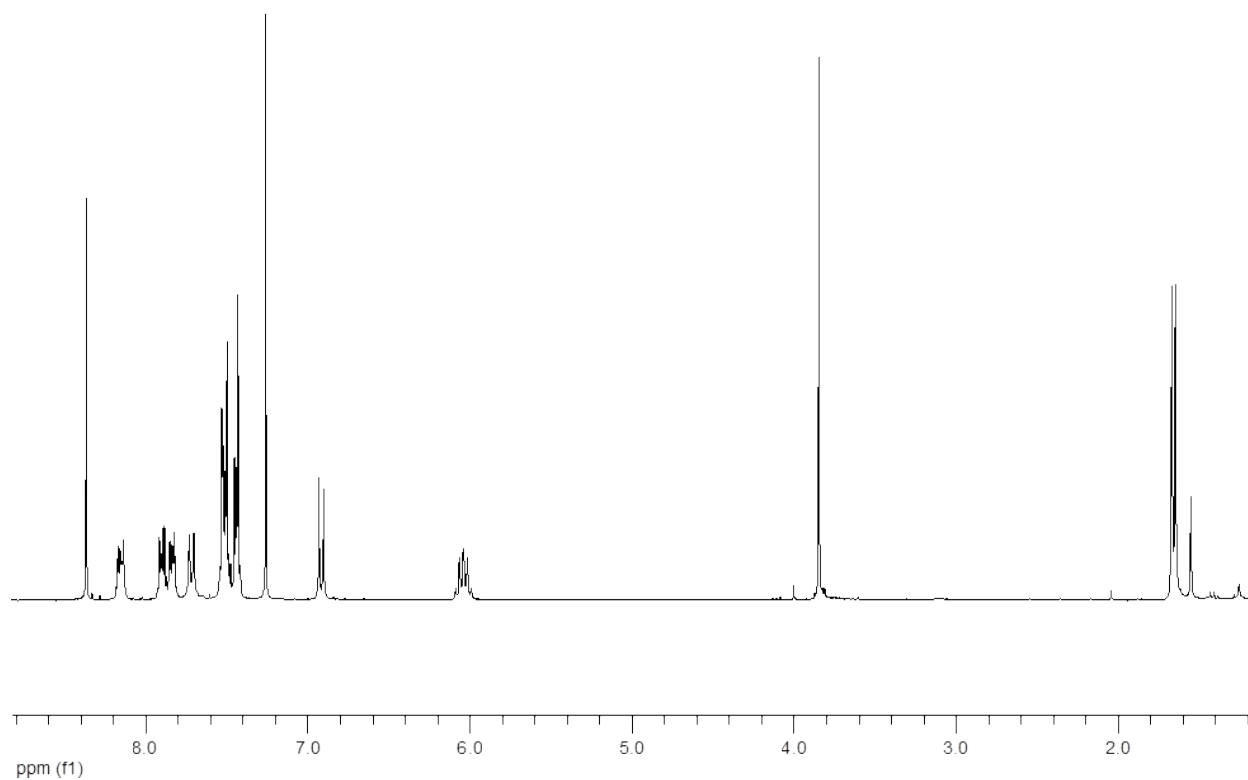


**Figure S22.** <sup>1</sup>H-NMR spectrum (300 MHz, CDCl<sub>3</sub>) of (*S,S*)-L ligand.

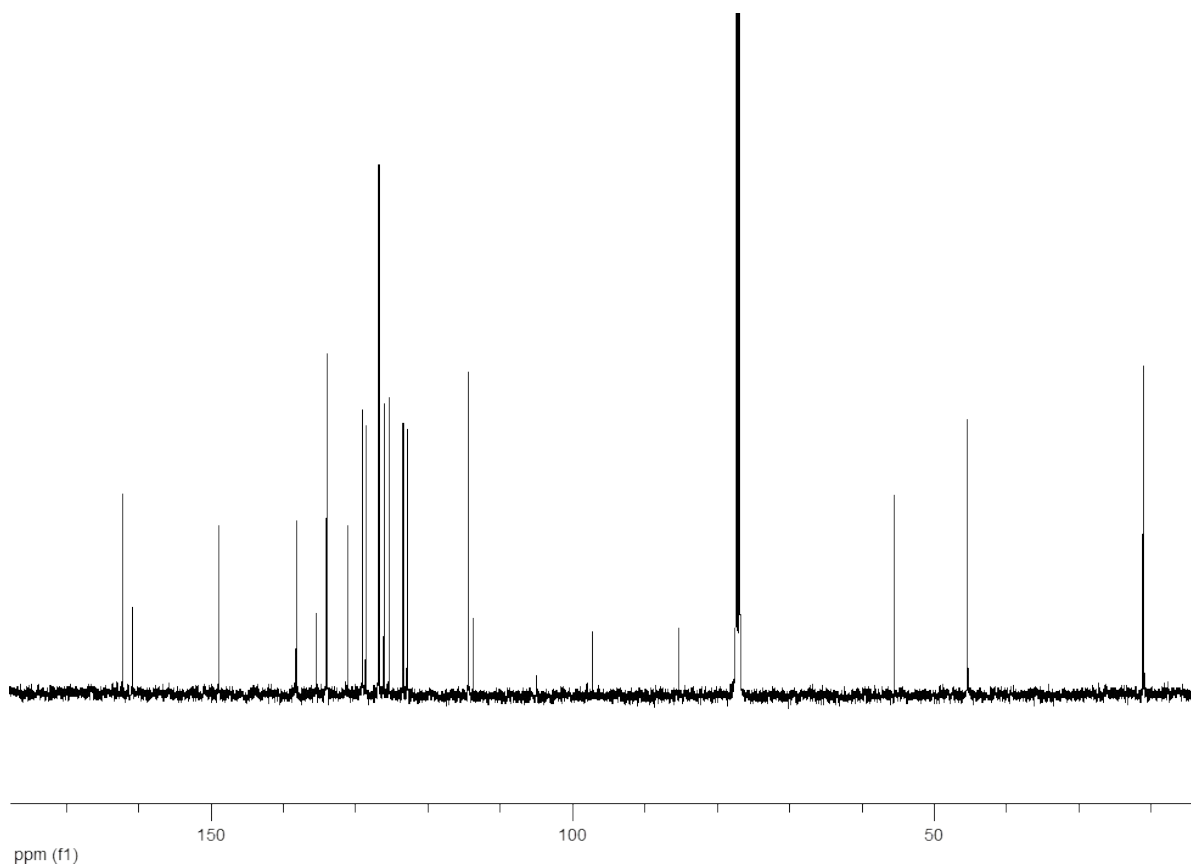


**Figure S23.** <sup>13</sup>C-NMR spectrum (125 MHz, CDCl<sub>3</sub>) of (*R,R*)-L ligand.

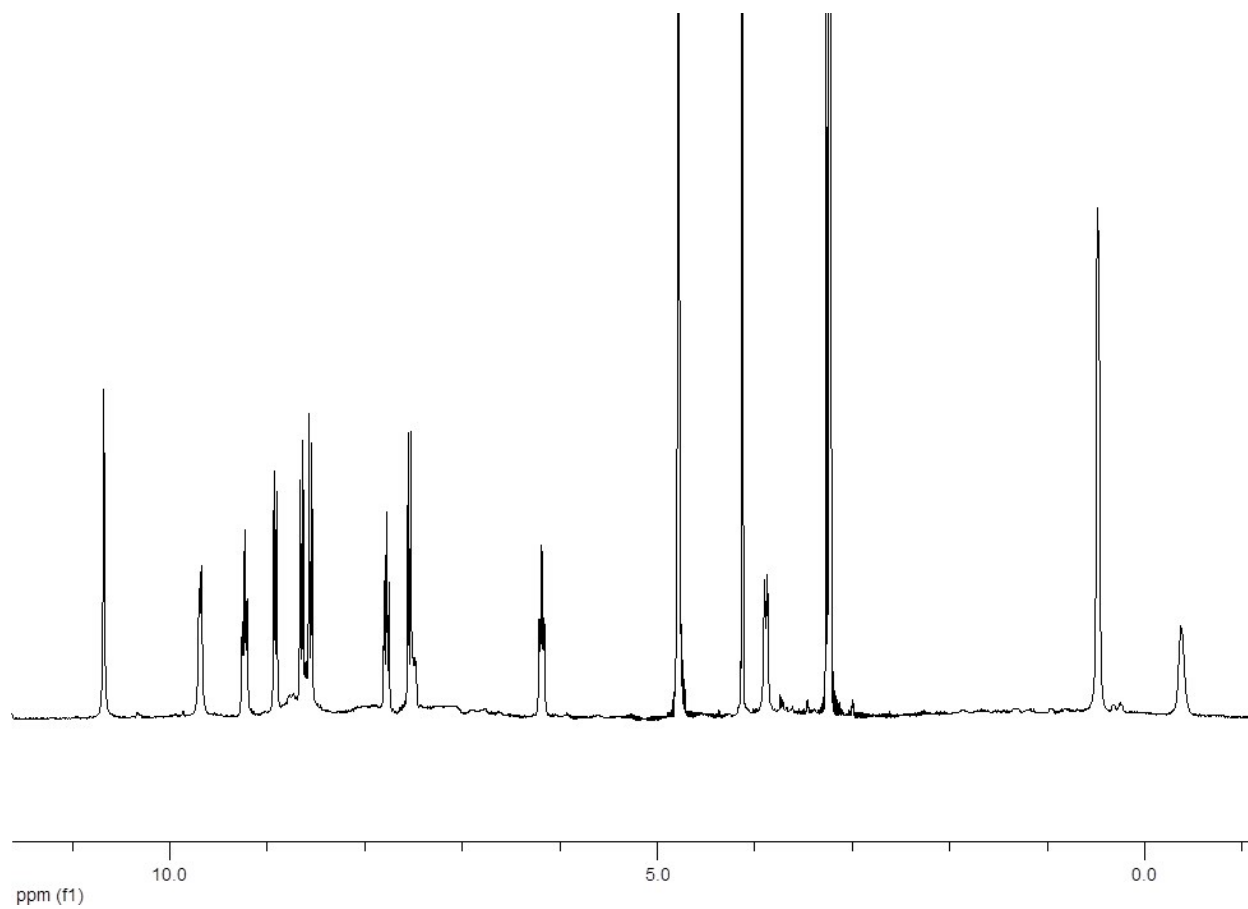


**Figure S24.**  $^1\text{H}$ -NMR spectrum (500 MHz,  $\text{CD}_3\text{OD}$ ) of  $[\text{Pr}(\text{S,S})\text{-L}_3]\text{Cl}_3$ .

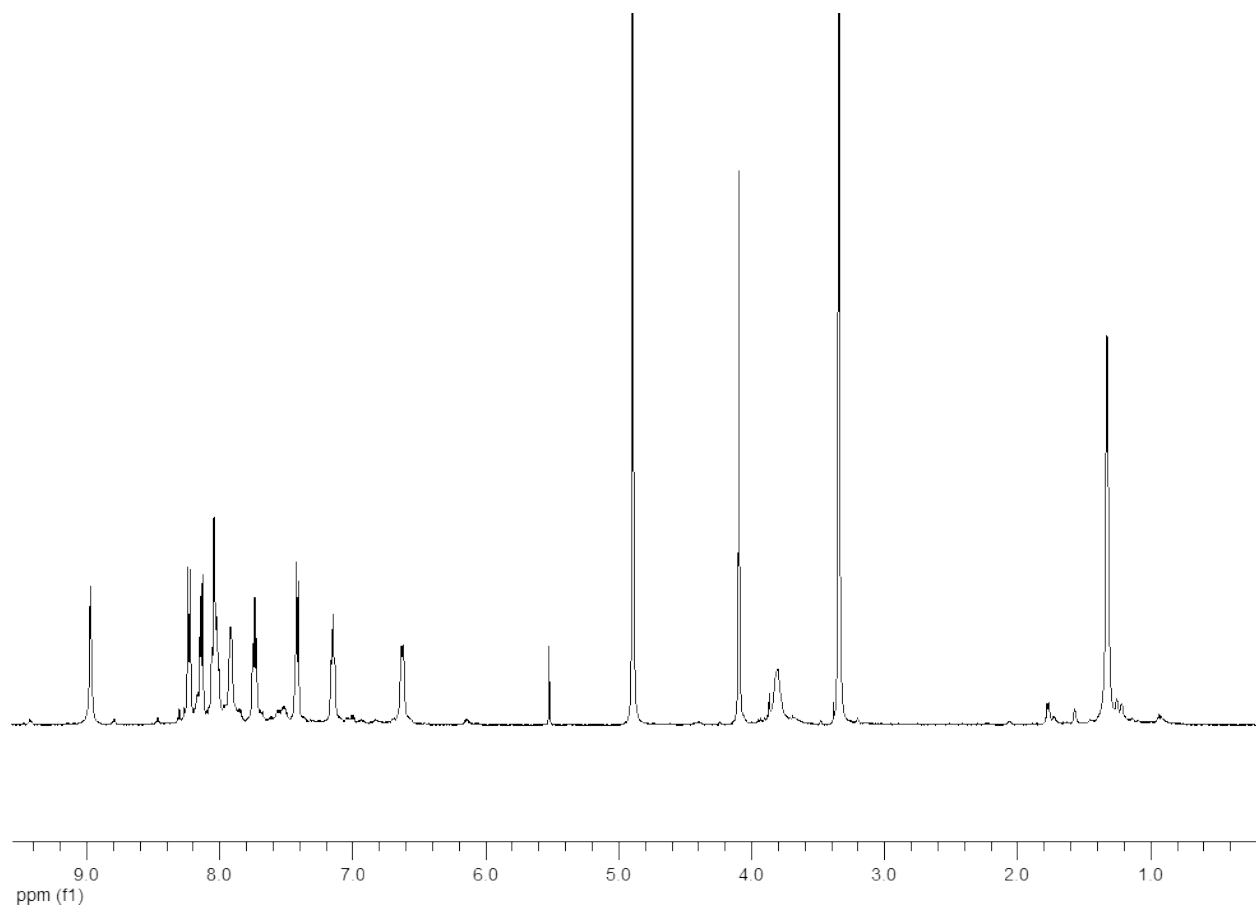


**Figure S25.**  $^1\text{H-NMR}$  spectrum (500 MHz,  $\text{CD}_3\text{OD}$ ) of  $[\text{Nd}(\text{R,R})\text{-L}_3](\text{OTf})_3$ .

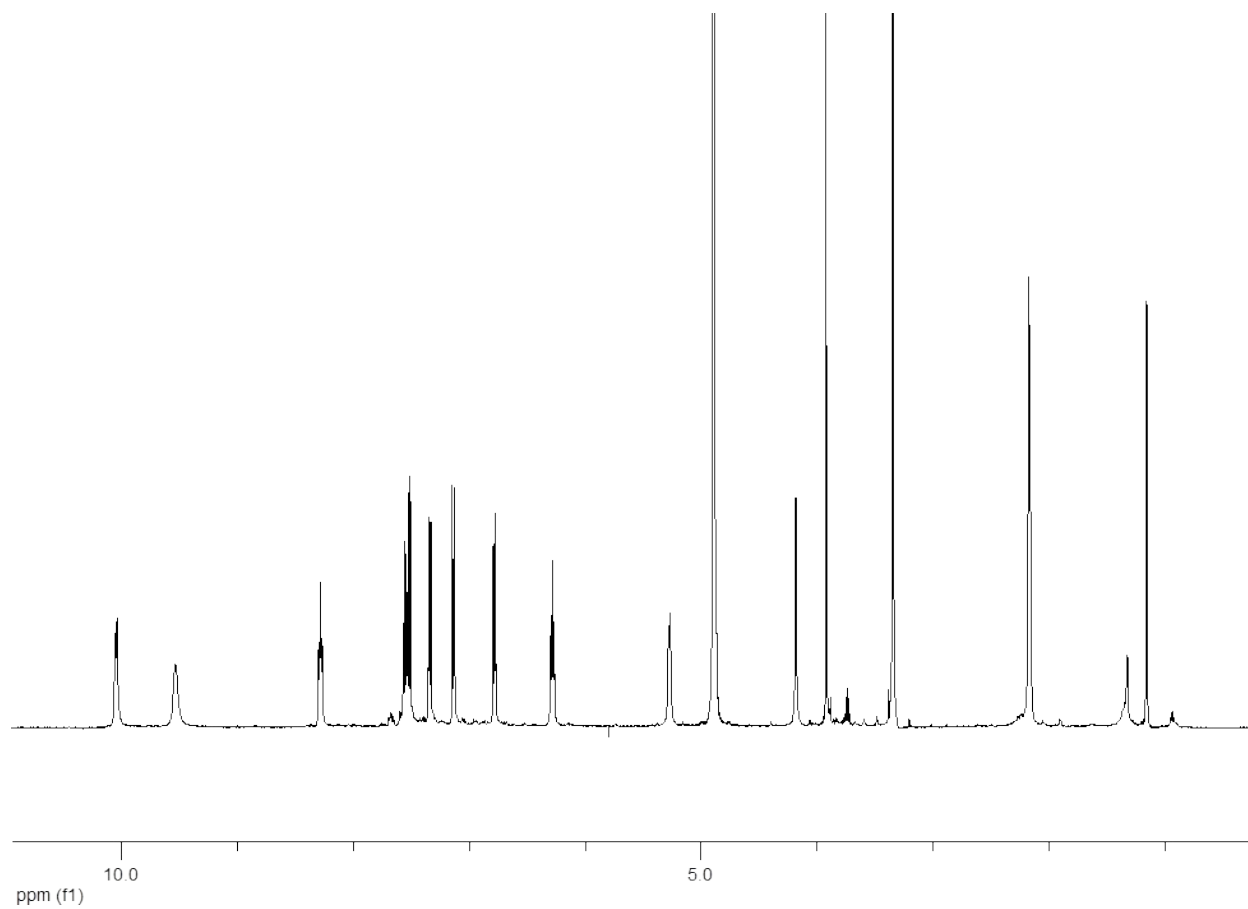


**Figure S26.**  $^1\text{H-NMR}$  spectrum (500 MHz,  $\text{CD}_3\text{OD}$ ) of  $[\text{Eu}(\mathbf{S,S}\text{-L}_3)](\text{OTf})_3$ .

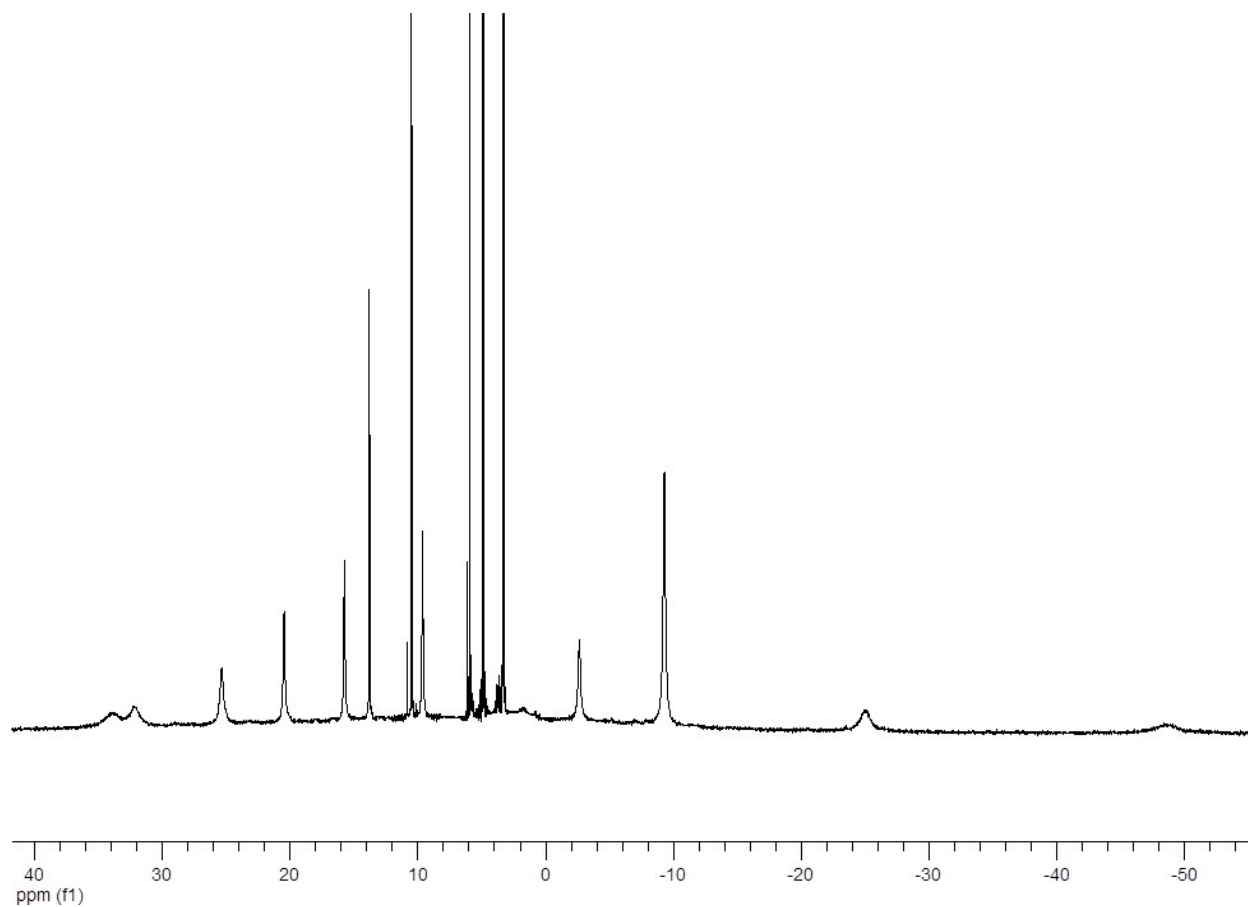


**Figure S27.** <sup>1</sup>H-NMR spectrum (500 MHz, CD<sub>3</sub>OD) of [Dy(*R,R*)-L<sub>3</sub>](NO<sub>3</sub>)<sub>3</sub>.

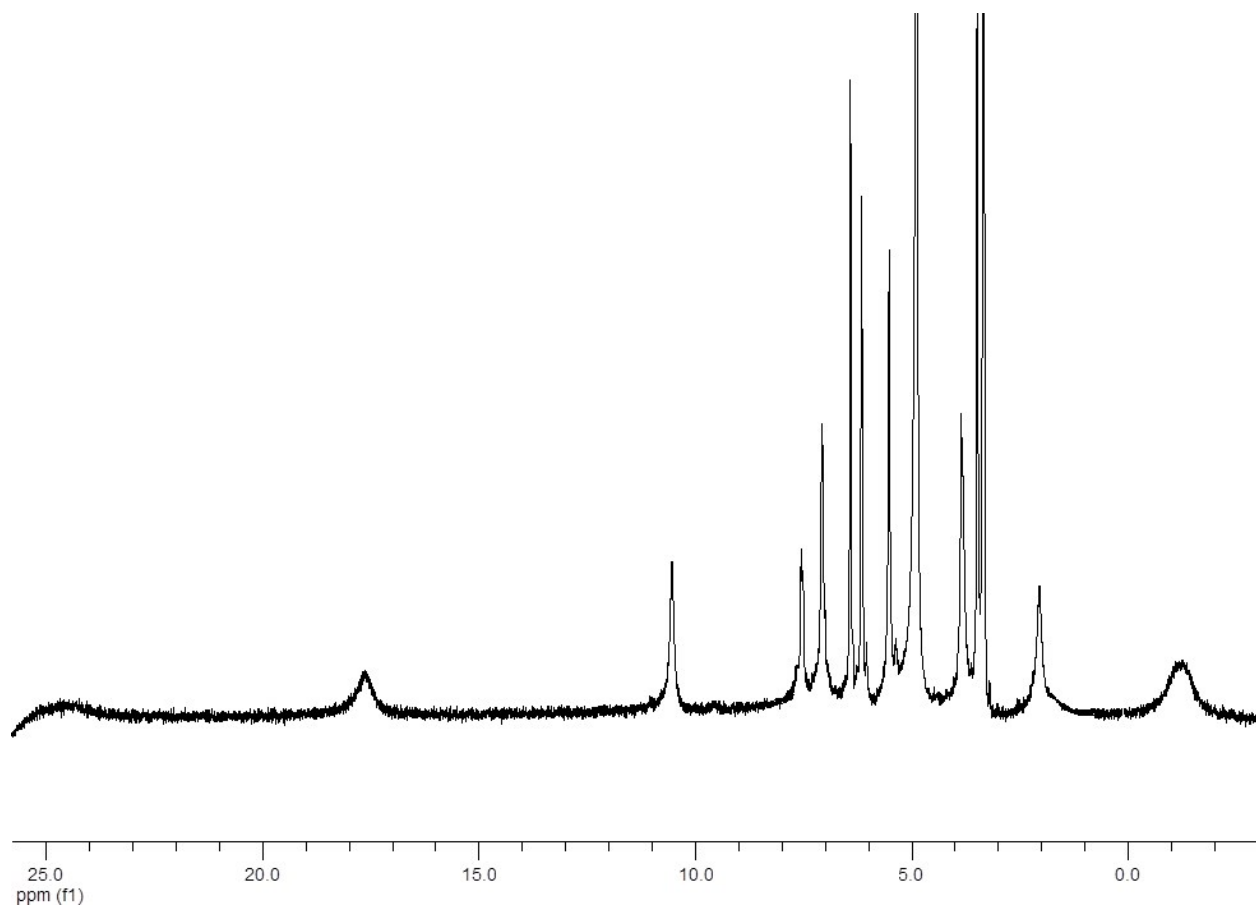


**Figure S28.** <sup>1</sup>H-NMR spectrum (500 MHz, CD<sub>3</sub>OD) of [Er(*R,R*-L<sub>3</sub>)(OTf)<sub>3</sub>].

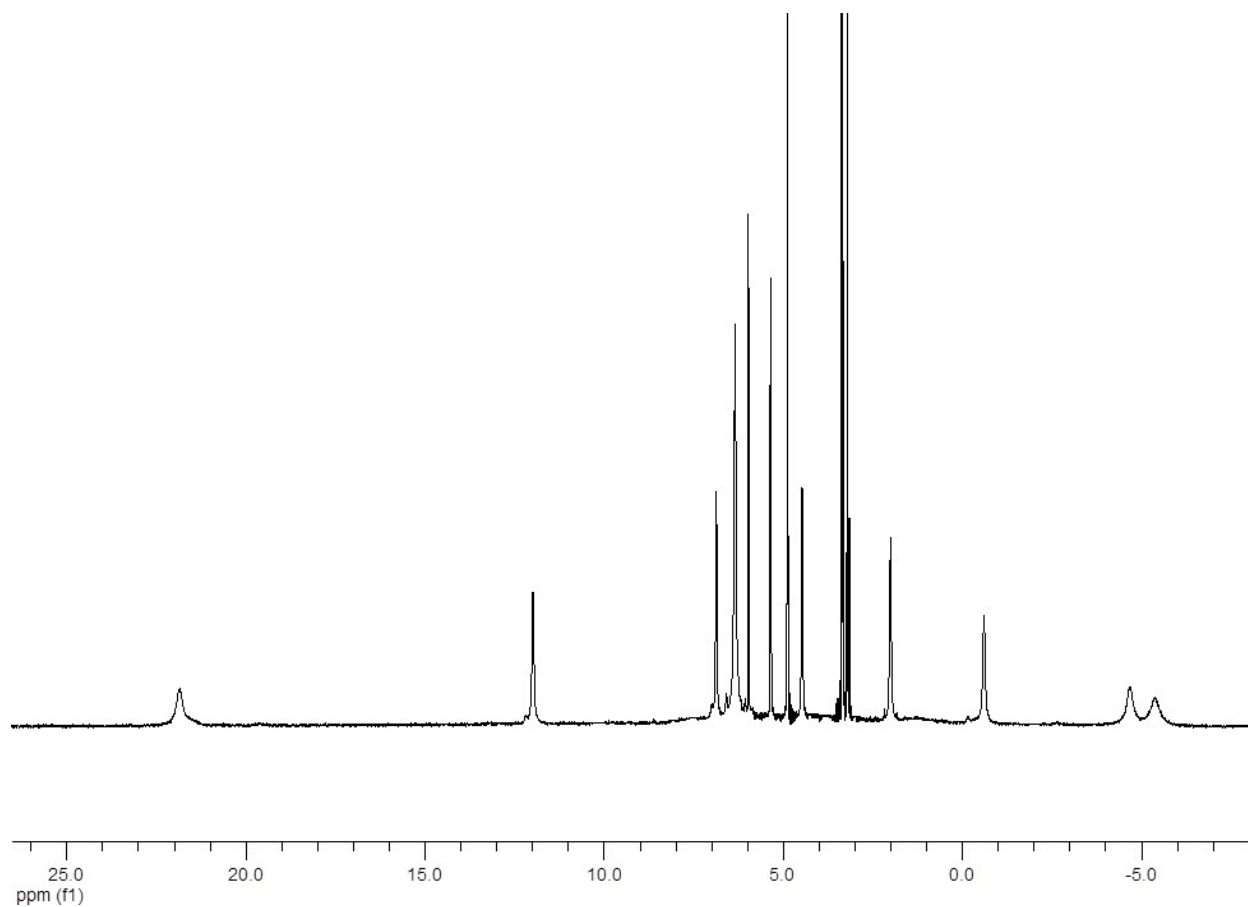


**Figure S29.** <sup>1</sup>H-NMR spectrum (500 MHz, CD<sub>3</sub>OD) of [Tm(*R,R*)-L<sub>3</sub>]Cl<sub>3</sub>.

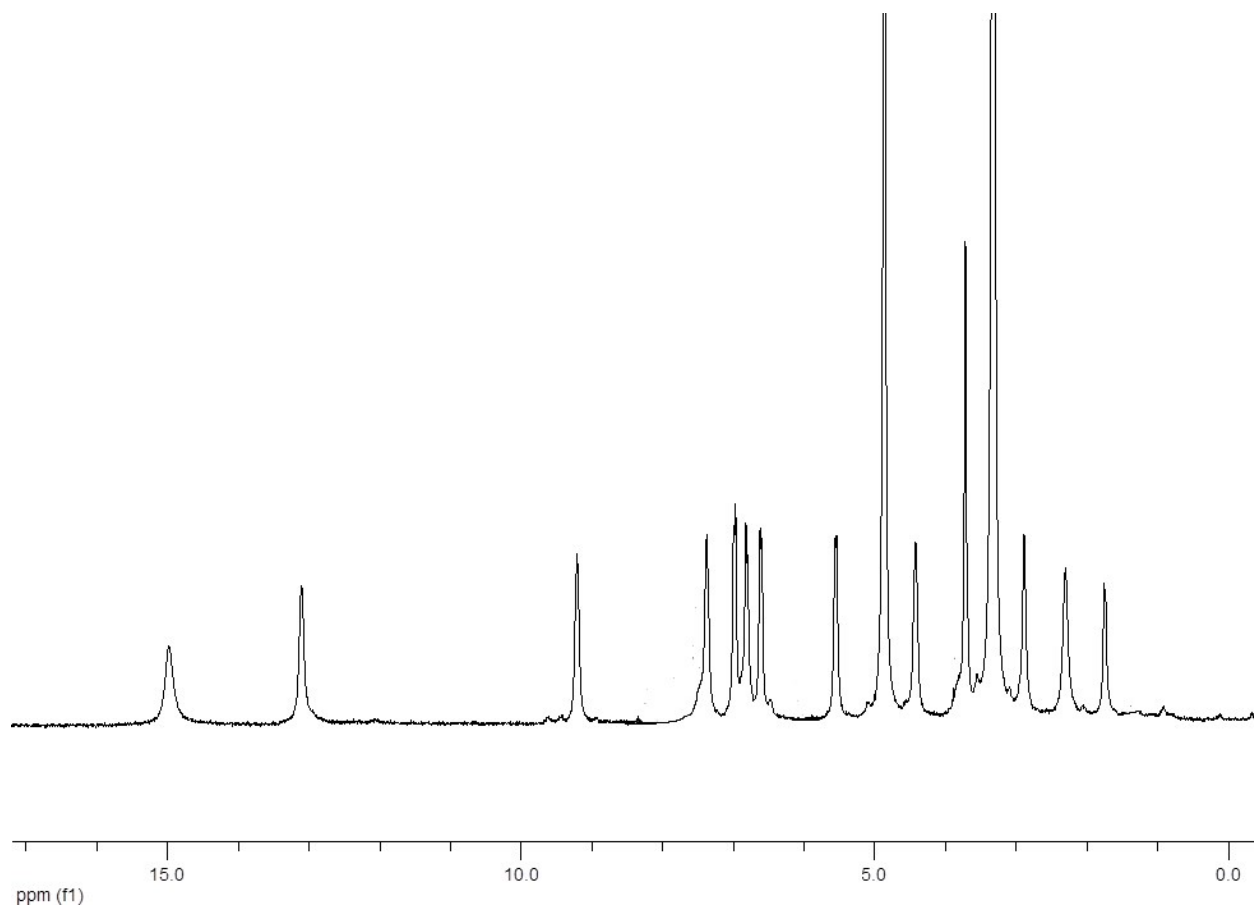


**Figure S30.**  $^1\text{H-NMR}$  spectrum (500 MHz,  $\text{CD}_3\text{OD}$ ) of  $[\text{Yb}(\mathbf{R,R}\text{-L}_3)](\text{OTf})_3$ .

## References

---

- 1 J. P. Leonard, P. Jensen, T. McCabe, J. E. O'Brien, R. D. Peacock, P. E. Kruger, T. Gunnlaugsson *J. Am. Chem. Soc.* 2007, **129**, 10986-10987.
- 2 L. Guy, M. Mosser, D. Pitrat, J.-C. Mulatier, M. Kukulka, M. Srebo-Hooper, E. Jeanneau, A. Bensalah-Ledoux, B. Baguenard, S. Guy *J. Org. Chem.* 2019, **84**, 10870-10876.
- 3 S. Guy, A. Bensalah-Ledoux, A. Lambert, Y. Guillin, L. Guy and J.-C. Mulatier *Thin Solid Films*, 2012, **520**, 6440-6445.
- 4 I. F. Galván, M. Vacher, A. Alavi, C. Angeli, F. Aquilante, J. Autschbach, J. J. Bao, S. I. Bokarev, N. A. Bogdanov, R. K. Carlson, L. F. Chibotaru, J. Creutzberg, N. Dattani, M. G. Delcey, S. S. Dong, A. Dreuw, L. Freitag, L. M. Frutos, L. Gagliardi, F. Gendron, A. Giussani, L. Gonzalez, G. Grell, M. Guo, C. E. Hoyer, M. Johansson, S. Keller, S. Knecht, G. Kovačević, E. Källman, G. Li Manni, M. Lundberg, Y. Ma, P.-Å. Malmqvist, P. Marquetand, S. A. Mewes, J. Norell, M. Olivucci, M. Oppel, Q. M. Phung, K. Pierloot, F. Plasser, M. Reiher, A. M. Sand, I. Schapiro, P. Sharma, C. J. Stein, L. K. Sørensen, D. G. Truhlar, M. Ugandi, L. Ungur, A. Valentini, S. Vancoillie, V. Veryazov, O. Weser, T. A. Wesolowski, P.-O. Widmark, S. Wouters, A. Zech, A. Zobel and R. Lindh *J. Comput. Chem.* 2019, **15**, 5925–5964.
- 5 B. O. Roos, P. R. Taylor and P. E. M. Siegbahn *Chem. Phys.* 1980, **48**, 157–173.
- 6 K. Andersson, P.-Å. Malmqvist, B. O. Roos, A. J. Sadlev and K. Wolinski, *J. Phys. Chem.* 1990, **94**, 5483–5488.
- 7 M. Douglas and N. M. Kroll, *Ann. Phys.* 1974, **82**, 89-155.
- 8 B. A. Hess *Phys. Rev. A* 1985, **32**, 756-763.
- 9 B. A. Hess *Phys. Rev. A* 1986, **33**, 3742-3748.
- 10 A. Wolf, M. Reiher and B. A. Hess *J. Chem. Phys.* **2002**, *117*, 9215-9226.
- 11 (a) P.-O. Widmark, P.-Å. Malmqvist and B. O. Roos, *Theor. Chim. Acta* 1990, **77**, 291–306; (b) B. O. Roos, R. Lindh, P.-Å. Malmqvist, V. Veryazov and P.-O. Widmark, *J. Phys. Chem. A* 2004, **108**, 2851–2858; (c) B. O. Roos, R. Lindh, P.-Å. Malmqvist, V. Veryazov and P.-O. Widmark, *J. Phys. Chem. A* 2005, **109**, 6575.
- 12 F. Gendron, B. Moore II, O. Cador, F. Pointillart, J. Autschbach, B. Le Guennic *J. Chem. Theory. Comput.* 2019, **15**, 4140-4155.
- 13 P.-A. Malmqvist, B. O. Roos and B. Schimmelpfennig, *Chem. Phys. Lett.* 2002, **357**, 230-240.
- 14 (a) H. Bolvin *ChemPhysChem* 2006, **7**, 1575-1589; (b) L. F. Chibotaru and L. Ungur *J. Chem. Phys.* 2012, **137**, 064112-22.
- 15 (a) F. Gendron, D. Pérez-Hernández, F.-P. Notter, B. Pritchard, H. Bolvin and J. Autschbach *Chem. Eur. J.* 2014, **20**, 7994–8011; (b) F. Gendron, B. Pritchard, H. Bolvin and J. Autschbach *Dalton Trans.* 2015, **44**, 19886– 19900; (c) F. Gendron H. Bolvin and J. Autschbach *Complete Active Space Wavefunction-Based Analysis of Magnetization and Electronic Structure*. In: Chandrasekhar V., Pointillart F. (eds) *Organometallic Magnets*. Topics in Organometallic Chemistry, **2018** vol 64. Springer, Cham
- 16 M. J. Frisch, G. W. Trucks, H. B. Schlegel, G. E. Scuseria, M. A. Robb, J. R. Cheeseman, G. Scalmani, V. Barone, B. Mennucci, G. A. Petersson, H. Nakatsuji, M. Caricato, X. Li, H. P. Hratchian, A. F. Izmaylov, J. Bloino, G. Zheng, J. L. Sonnenberg, M. Hada, M. Ehara, K. Toyota, R. Fukuda, J. Hasegawa, M. Ishida, T. Nakajima, Y. Honda, O. Kitao, H. Nakai, T. Vreven, J. A. Montgomery, Jr., J. E. Peralta, F. Ogliaro, M. Bearpark, J. J. Heyd, E. Brothers, K. N. Kudin, V. N. Staroverov, R. Kobayashi, J. Normand, K. Raghavachari, A. Rendell, J. C. Burant, S. S. Iyengar, J. Tomasi, M. Cossi, N. Rega, J. M. Millam, M. Klene, J. E. Knox, J. B. Cross, V. Bakken, C. Adamo, J. Jaramillo, R. Gomperts, R. E. Stratmann, O. Yazyev, A. J. Austin, R. Cammi, C. Pomelli, J. W. Ochterski, R. L. Martin, K. Morokuma, V. G. Zakrzewski, G. A. Voth, P. Salvador, J. J. Dannenberg, S. Dapprich, A. D. Daniels, Ö. Farkas, J. B.

---

Foresman, J. V. Ortiz, J. Cioslowski, and D. J. Fox, *Gaussian 09* (Gaussian, Inc., Wallingford CT, 2009)  
17 a) C. Lee, W. Yang and R. G. Parr, *Phys. Rev. B* 1988, **37**, 785–789; b) A. D. Becke *J. Chem. Phys.* 1993, **98**, 5648–5652.  
18 S. Di Pietro, S. Lo Piano and L. Di Bari *Coord. Chem. Rev.* 2011, **255**, 2810-2820.